

Asymmetric nickel-doped chromium molybdates
(Ni_x Cr_{2-x} (MoO₄)₃ as high-performance anode materials for
supercapacitors



Maqdoona Zahra

Reg. No. (00000330912)

A thesis in partial fulfillment of the requirements for the degree of
Master of Science (MS)

In

Chemistry

Supervised by: Dr. Asad Mumtaz

Department of Chemistry

School of Natural Sciences

National University of Science and Technology H-12,

(2023)

THESIS ACCEPTANCE CERTIFICATE


Certified that final copy of MS thesis written by Maqdoona Zahra (Registration No. 00000330912), of School of Natural Sciences has been vetted by undersigned, found complete in all respects as per NUST statutes/regulations, is free of plagiarism, errors, and mistakes and is accepted as partial fulfillment for award of MS/M.Phil degree. It is further certified that necessary amendments as pointed out by GEC members and external examiner of the scholar have also been incorporated in the said thesis.

Signature: 

Name of Supervisor: Dr. Asad Mumtaz

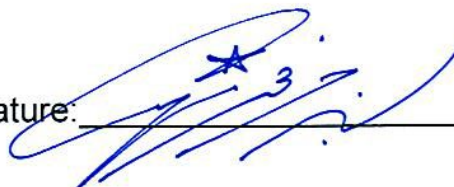

Date: _____

Signature (HoD): 
Date: 20/6/23

Signature (Dean/Principal): 
Date: 20/6/2023

National University of Sciences & Technology**MS THESIS WORK**

We hereby recommend that the dissertation prepared under our supervision by: Maqdoona Zahra, Regn No. 00000330912 Titled: Asymmetric Nickle-Doped Chromium Molybdates ($Ni_xCr_{2-x}(MoO_4)_3$ as High-Performance Anode Materials for Supercapacitors be Accepted in partial fulfillment of the requirements for the award of **MS** degree.

Examination Committee Members1. Name: PROF. AZHAR MAHMOODSignature: 2. Name: PROF. MANZAR SOHAILSignature: Supervisor's Name DR. ASAD MUMTAZSignature: 

 Head of Department

20/6/23
 Date
COUNTERSIGNEDDate: 20/6/2023

 At Dean/Principal

DEDICATION

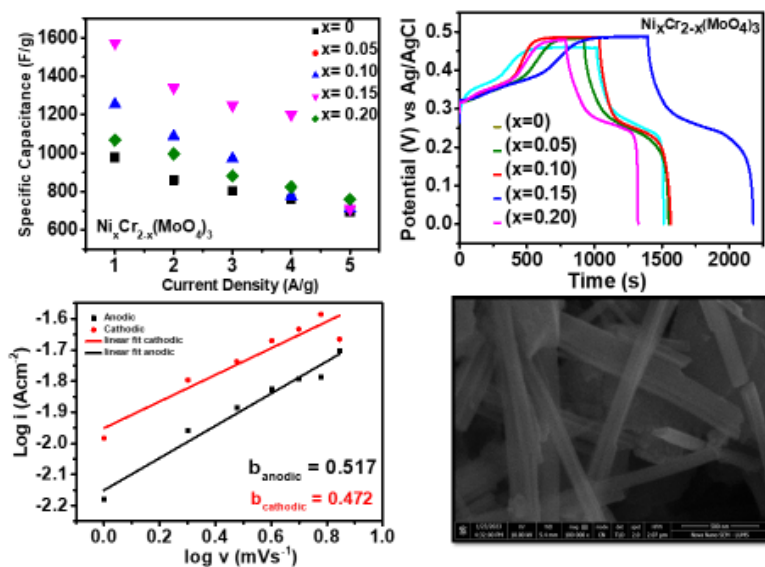
I AFFECTIONATELY DEDICATE THIS EFFORT TO ALL THE MEMBERS OF MY HONOURABLE FAMILY, ESPECIALLY TO MY PARENTS, NOT FORGETTING MY RESPECTED TEACHERS AND FRIENDS, WHO HAD A REMARKABLE EFFORT IN THIS ACHIEVEMENT.

"Basic Research is what I am doing when I don't know what I am doing".

WERNHER VON BRAUN

ABSTRACT

In this work, Nickel-doped Chromium Molybdates were synthesized by a convenient, cost-effective, and good-yield co-precipitation process for supercapacitor electrodes. Morphological and structural characterizations of materials were carried out by using scanning electron microscopy (SEM), energy dispersive spectroscopy (EDS), X-ray diffraction (XRD), and Raman spectroscopy. The electrochemical performance was evaluated by performing cyclic voltammetry, galvanostatic charge-discharge, and electrochemical impedance spectroscopy. Based on the synergistic effect of both Ni (II) and Cr (III) ions, specific capacitance increases with the doping of nickel until the parent lattice structure is maintained. The material with a nickel dopant concentration of 0.15 delivered the highest specific capacitance of 1572 F/g at 1 A/g among all other materials, good cyclic stability, and 100% coulombic efficiency. Moreover, the detailed kinetic analyses suggested that the dominance of the diffusion-controlled charge storage mechanism is responsible for the high specific capacitance of the materials. The present study demonstrated the traits of materials as potential anodes for designing high-performance asymmetric supercapacitors and also provided new insights for the development of high-performance materials for supercapacitors by using simple synthetic approach.



ACKNOWLEDGEMENTS

BISMILLAHIRRAHMANIRRAHIM

Alhamdulillah, Praise be to Allah Almighty for the help and guidance that finally made me able to complete this thesis. First and foremost, I offer my sincerest gratitude to my supervisor **Dr. Asad Mumtaz**, Assistant Professor, who has advised and guided me throughout my research with his patience and deepest knowledge.

- ❖ I would like to give my special thanks to my **friends** for sharing the ups and down throughout the completion of my research work and thesis. I pay my special regards and a lot of thanks to my **classmates** for their encouragement and support, especially at times when things were going tough.
- ❖ I cannot end without saying thanks to my family members, especially to my **parents** who supported me financially and encouraged me during my research work.

I hope, these studies will benefit to all of us.

Maqdoona Zahra

TABLE OF CONTENTS

ABSTRACT	I
TABLE OF CONTENTS	II
LIST OF ABBREVIATIONS	V
LIST OF FIGURES	VI
LIST OF TABLES	VII
CHAPTER 1: INTRODUCTION	1
1.1 Requirement of Energy Storage Systems.....	2
1.2 Types of Energy Storing Systems.....	3
1.3 Batteries.....	4
1.3.1 Primary Battery.....	5
1.3.2 Secondary Battery.....	5
1.3.2.1 Lithium-ion battery.....	6
1.3.2.2 Ni-Metal hydride battery.....	6
1.3.2.3 Ni-Cadmium battery.....	7
1.3.2.4 Lead-acid batteries.....	7
1.4 Fuel Cells.....	8
1.5 Supercapacitors.....	10
1.6 Types of supercapacitors.....	10
1.6.1 Symmetrical Supercapacitor.....	11
1.6.2 Asymmetrical Supercapacitor.....	12
1.6.3 Electric double layer capacitor (EDLC).....	13
1.6.4 Pseudocapacitor.....	14
1.7 EDLCs vs Pseudocapacitors.....	14
1.8 Pseudocapacitive materials.....	15
1.9 Molybdates.....	16
1.10 Aims And Objectives.....	19
CHAPTER 2: LITERATURE REVIEW	21
CHAPTER 3: MATERIALS AND METHODS	28
3.1 Materials.....	29
3.2 Synthesis.....	30
CHAPTER 4: CHARACTERIZATION	38
4.1 Introduction to Characterization Techniques.....	39
4.1.1 X-ray Diffraction.....	40
4.1.2 Raman Spectroscopy	42

4.1.3 Scanning Electron microscopy	
4.1.4 Energy dispersive X-rays Spectroscopy (EDS).....	44
4.2 Electrochemical Evaluation.....	46
CHAPTER 5: RESULTS AND DISCUSSIONS	48
CHAPTER 6: CONCLUSIONS	63
REFERENCES	64

LIST OF ABBREVIATIONS

XRD	:	X-ray Diffraction
EIS	:	Electrochemical Impedance Spectroscopy
DI	:	Deionized
CNT	:	Carbon Nano Tubes

LIST OF FIGURES

Figure 1.1 Concept of Energy Storage.....	6
Figure 1.1.1 Categorization of energy storing systems.....	10
Figure 1.1.2 Basic structure of Hydrogen fuel cell.....	20
Figure 1.1.3 Major factors affecting the performance of supercapacitor.....	27
Figure 1.3.1. Schematic scheme depicting the synthesis of chromium molybdate.....	35
Figure 1.3.2 Schematic Scheme showing the synthesis of nickel Doped Chromium Molybdates.....	35
Figure 1.4.1 Configuration of SEM.....	42
Figure 5.1. SEM images of $x=0$	47
Figure 5.2. SEM images of $x=0.05$	47
Figure 5.3 SEM images of $x=0.10$	48
Figure 5.4 SEM images of $X=0.15$	48
Figure 5.5 SEM images of $x=0.20$	49
Figure 5.6 EDS graphs	50
Figure 5.7 (a) XRD patterns and (b) Raman spectra of all the samples.....	52
Figure 5.8 Cyclic voltammetry profiles.....	52
Figure 5.9 (a) CV recorded for kinetic studies (b) relationship between $\log i$ and $\log v$	55
Figure 5.1.1 shows (a) specific capacitance values at different current densities (b) EIS (c) Capacitance retention and Coulombic Efficiency.....	56

LIST OF TABLES

Table 1. Specific capacitance calculated from CV profiles of all the materials at 5 mVsec ⁻¹	45
Table 2. Specific capacitance calculated from equation (2)	46
Table 3. . EIS fitting data	56
Table 4. Comparative review	57

CHAPTER 1: INTRODUCTION

Energy is a key factor in boosting a country's economy and is seen as a vital indication of the economic and social progress of any country. Undoubtedly, at this time, no nation can grow its economy without successfully balancing supply and demand. Compared to 2016, the total amount of energy used grew by 2.3% in 2017. According to statistics, the United States' energy use is 97 Btu, China's 139 quadrillions Btu, Russia's 32 Btu, and India's 30 Btu[1].

The burning of fossil fuels harms the environment by causing air pollution. The use of fossil fuels has an adverse effect on human health, which raises healthcare costs and decreases workday productivity for everyone in the world. Some researchers [2, 3] looked into how disruptions in the agricultural sector due to climate change can result in food insecurity by raising temperatures, causing droughts, and depleting water supplies. Clean air is a basic requirement for humanity to thrive on the planet, just as food and water are for the continuation of life.

There has been a sharp rise in environmental concerns around the world, and tragically no region or country is exempted from the adversities of climate change. Developing countries are intending to gain exponential economic progress for which unsustainable fuel consumption is not unusual. As a result, developed countries are experiencing ecological deficits due to high demands and continuous fuel consumption. The most developed group of countries are confronting growing climate change and ecological degradation challenges.[4]

1.2 Requirement of Energy Storage Systems

A machine that turns energy from a certain type, often electrical power, to another that can be held and then turned back to electricity when appropriate is known as a system for the storage of energy. Storage system typically finds use in electrical lines, handheld devices, and vehicles. The power grid uses energy storage devices for several purposes, such as electricity time-shifting, capacity for electric supply, frequency, and voltage support, and electricity bill control. Currently, only a small amount of electric energy is produced using renewable resources. The fluctuating demand for grids of electric power has the ability to absorb all the generated energy from renewable sources. It has been observed that when the energy obtained from solar and wind sources exceeds the limit of 25-30% of the total produced energy, the demand for energy (electric) stoops to extremely low values and sometimes even turns negative. [5]. This suggests that the requirement for the energy generated by solar and wind power is not achievable. Moreover, as electric vehicles become more prevalent, the traditional reliance on petrochemicals is expected to be disrupted, potentially transforming personal mobility. Demand management, behind-the-meter storage, and distributed energy resources like rooftop solar are all changing how the transmission and distribution system functions. During these times, energy storage is vital. The fact that most renewable energy sources—especially sun and wind—occur periodically and are therefore unreliable for consistent energy delivery is one of their biggest challenges. These renewable resources can be transformed into dependable and consistent energy sources by utilizing the energy storage idea. This is possible when the extra energy produced is stored when solar and wind resources are present and then using that energy again when those resources are unavailable.



Figure 1.1 Concept of Energy Storage [6]

1.3 Types of Energy Storing Systems

Energy storing technologies are mainly categorized into (a) Electrical (b) and thermal energy storing systems.

(a) The electrical energy depositing systems are further categorized as

1. Mechanical energy storage systems

- Flywheel
- Liquid piston
- Pumped Hydro gravity
- Compressed Air

2. Chemical energy storage systems

- Biofuel
- Biodiesel
- Hydrogen

3. Electrochemical energy storage systems

- Supercapacitors
- Batteries
- Fuel Cells

4. Superconducting magnetic energy storage systems

5. Cryogenic energy storage systems

- Liquid Air

(b) Thermal energy storage systems

1. Sensing heat storage

- Ceramics
- Chilled water

- Concrete
 - Molten salts
2. Latent heat storage
 - Phase change minerals
 - Ice
 3. Thermochemical heat storage

Here, in this work supercapacitors are focused which is on electrochemical energy storage systems the relation of it them with different electrochemical energy storing systems will be discussed.

1.4 Batteries

An electrochemical cell, or group of cells, that generates an electric current, is a battery. There are two main types of batteries.

- ❖ Secondary battery
- ❖ Primary battery

1.4.1 Primary Battery

Primary batteries are non-rechargeable types of energy-storing devices. Zinc-carbon battery, also known as dry cell is a common type of battery. Here, the negative electrode is the zinc container which acts as both a shield and an electrode while the carbon rod is a positive electrode. It delivers a cell potential of 1.5V, which decreases with time. This type of battery should not be left in the electrical devices because, with the oxidation of the zinc container, the material inside it leaks out and damages the devices.

An alkaline battery is another example of a primary battery. In this potassium hydroxide act as an electrolyte.

1.4.2 Secondary Battery

Secondary batteries are rechargeable devices that deliver an excellent output of energy density and are thus widely used in vehicles, mobiles, and laptops.

1.4.2.1 Lithium-ion battery

The working of the Li-ion in portable electronics and medical equipment has been demonstrated to be good. The Li-ion battery is recyclable, exhibits a good energy density, and performs well at high temperatures. The negative electrode is constructed of carbon, whereas the positive electrode is constructed from oxidized cobalt. The electrolytic medium is comprised of the Li salt dissolved in any of the soluble solvents. The advantages of the Li-ion battery include power of 280 W/kg, low memory effect, energy of 120 Wh/kg, and durable shelf life of 2000 cycles [7].

1.4.2.2 Ni-Metal hydride battery

The cathode of a Ni-M-H battery is made of Ni (OH)₂ whereas anode is made of a designed alloy of nickel, titanium, vanadium, and a small number of metals. The Ni-M-H battery has twice as high energy density as a lead-acid battery. Ni-M-H batteries may be recycled, and their constituent parts are safe for the environment. The Ni-M-H battery is secure to be used at high ranges of voltage and has a lot of other benefits, including the ability to store specific energy and power, have durable cyclic stability, function in a large range of temperatures, and be resistant to over-charging and over-discharging[8, 9].

1.4.2.3 Ni-Cadmium battery

Batteries made of Ni-Cd last a very long period and can be fully discharged without suffering any harm. Ni-Cd batteries have a specific energy density that varies from 50-60 Wh/kg [9]. These batteries have the benefit of recycling, but cadmium is a heavy metal that, if not disposed of properly, might pollute the environment. The high price of Ni-Cd batteries is another flaw.

1.4.2.4 Lead-acid batteries

PbO₂ serves as the battery's active material for the anode, spongy lead serves as its active material for the cathode, and H₂SO₄ serves as the electrolytic medium. Both anodic and cathodic elements are converted into PbSO₄ after the discharge. They may now be produced in large quantities, producing a power source that is

quite inexpensive. The lead-acid battery, however, is not recommended to use discharges that are more than 25% of its initial capacity. It suffers from low energy and power density due to the weight of collectors which are made of lead is high.

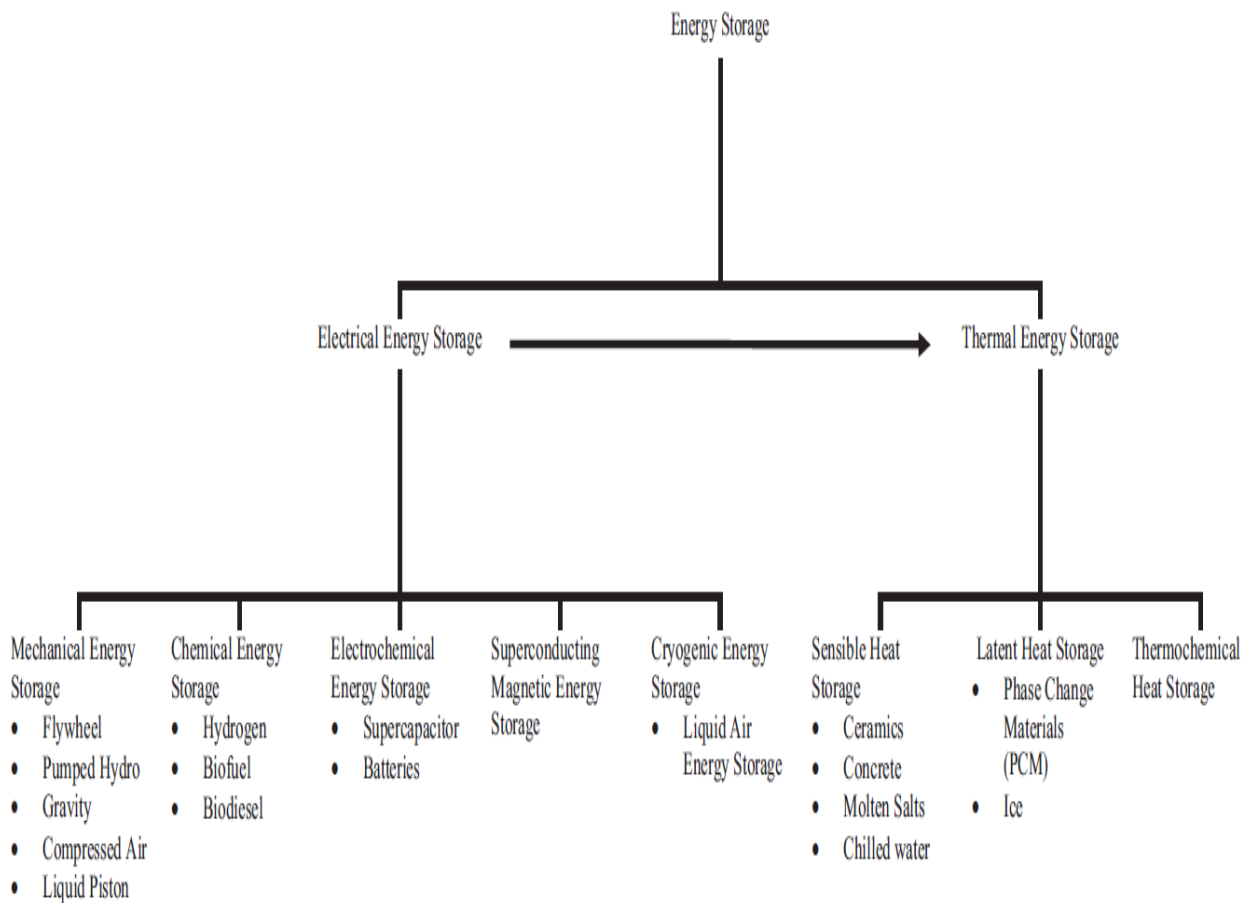


Figure 1.2. Categorization of energy storing systems [10]

1.5 Fuel Cells

A gadget in which one form of energy is transformed into electricity is known as fuel a cell. In contrast with the batteries, a constant supply of fuel, often hydrogen is required in the fuel cells. If a fuel is present in the cell, it will continue to create power.

In the cell, the reaction continues, and the reactants enter in the cell whereas products exit the cell. When the reactants, oxidants, and fuels have continuous flows, the fuel cell can produce power. A gas-flow stream delivers molecular hydrogen (H_2) to the anode, where it interacts electrochemically. To create hydrogen ions and electrons, the hydrogen is oxidized. Water is created at the cathode when oxygen from an external gas flow stream reacts with electrons and hydrogen ions.

High efficiency for the conversion of fuel into electricity, silent working, recovery of wasted heat, negligible or very low emission, flexibility for fuel, long shelf life, and dependability are all benefits of fuel cells[11]. Nevertheless, because of the narrow surface area of contact between the electrodes, electrolyte, and gas, fuel cells frequently only generate extremely modest amounts of current. The spacing between electrodes should also be taken into account. A thin electrolyte layer with flat porous electrodes is taken into consideration for the electrolyte and the gas penetration for increasing the surface area ultimately increasing the fuel cell efficiency[12].

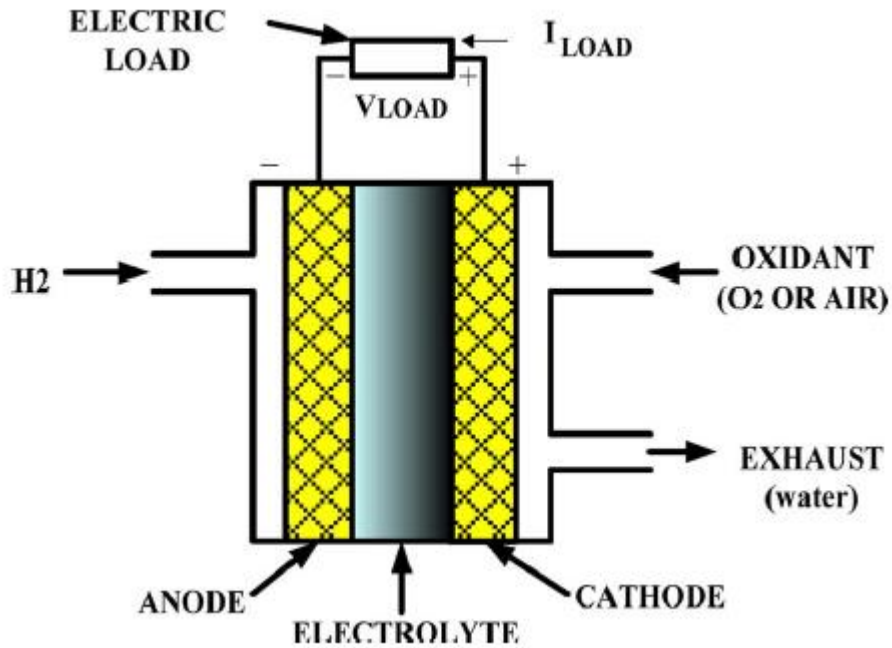


Figure 1.3. The basic structure of Hydrogen fuel cell [13]

1.6 Supercapacitors

When testing with devices that used porous carbon electrodes in 1957, some electrical engineers discovered the electric double layer capacitor (EDLC) phenomenon. They noticed that carbon pores were the place of energy storage, thereby providing incredibly high values of capacitance. Around 1967, while carrying on research at fuel cell prototypes, a team of researchers at Standard Oil of Ohio unintentionally discovered the phenomenon.

The name "supercapacitor" was ultimately introduced by NEC in 1979, and it was utilised to supply backup for preserving memory of computer.

The properties and functionality of supercapacitors are the consequence of the interaction between its working electrode and electrolytic ions. Different forms of carbon containing materials like aerogel, in various forms are typically used as the material for the fabrication of electrode for EDLC. Every type of material cannot be used for pseudocapacitors, generally, conducting polymers exhibiting low ESR, long

cyclic stability and high specific capacitance are used as pseudocapacitive materials. The hybrid supercapacitor is fabricated from two different electrodes, one with a significant EDLC character and other with pseudocapacitive behaviour. The fabrication of hybrid-type supercapacitor electrodes had a positive impact on rechargeable battery electrodes.

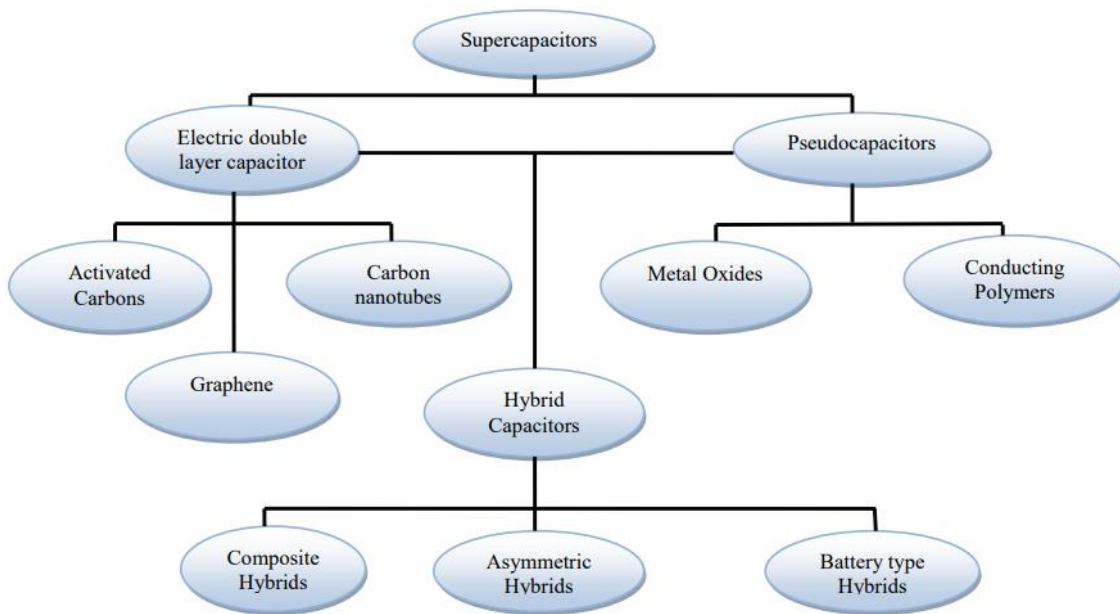


Figure 1.4. Categorization of supercapacitors

1.7 Types of supercapacitors

- ❖ Based on the fabrication pattern, supercapacitors have two types (a) symmetrical and (b) asymmetrical supercapacitors

1.7.1 Symmetrical Supercapacitor:

It is the most typical kind and contains two carbon electrodes comprised of the same active material that are symmetrically arranged. The capacitance of the two electrodes is roughly similar because the ratio anions to

cations is roughly same. The analogous circuit which is comprised of two same capacitors which are connected in series.

Many investigations focus on substituting the carbon electrode with redox active materials or pseudocapacitive (oxides or nitrides) materials that exhibit increased capacitance as a result of their charge storage mechanism. However, this rise in the cell's total capacitance typically coincides with declines in power density and cycle life.

1.7.2 Asymmetrical Supercapacitor:

Another type of electrodes combines the benefits of the EDLC in terms of good cyclic stability and excellent conductivity due to carbon materials and fast redox reactions that display faradaic behaviour.

The electrochemical behaviour of these supercapacitors typically exhibits the properties of fast kinetics and high specific capacitance due to the faradaic reactions and high energy density, durability, retention, and great cycling stability because of mechanisms involved in EDLC. Covalent bonding or p-p interactions with the carbon-based organic moieties have a significant advantage in this regard as the adherence of material to the surface of electrode is the main requirement for the good cyclic stability.

❖ Depending on the differences in charge-storage mechanism, supercapacitors are categorized into two main classes.

1.7.3 Electric double layer capacitor (EDLC)

In an EDLC (electric double layer supercapacitor), electrostatic energy gets deposited in the form of Helmholtz double layer at the junction of conductive electrode and electrolyte. Higher surface area is the main factor in determining the capacitance of EDLCs. Carbon and carbon derivatives are used for the EDLC. Such supercapacitors have high cyclic stability but low energy density.

1.7.4 Pseudocapacitor

Electrochemical energy storage which is known as false or pseudocapacitors involves the storage of charge which is accomplished by redox reactions on the surface with an aid of electrolytic ions, deposition of

hydrogen or metal on the lattice sites of the electrode surface, and intercalation of atoms which results in a reversible faradaic reaction. Pseudo- or false capacitors typically exhibit higher energy density than EDLCs.

1.8 EDLCs vs Pseudocapacitors

EDLCs which are what conventional supercapacitors are known as, are non-faradaic devices with an electrochemical signature that is primarily derived from the potential resistance of charges stored electrostatically at the surface of electrodes. The device generally produces power densities (16 kW/kg) with an energy density (5-12 Wh/kg) thanks to the most cutting-edge carbon electrode materials. Pseudocapacitive materials have electrochemical properties that are neither bulk Faradaic nor completely capacitive. Between EDLCs and batteries, pseudocapacitors, by definition, depend basically on the Faradaic electron transfer reactions at the surface.

1.9 Pseudocapacitive materials

There are a lot of materials which serve as supercapacitor electrodes and display significant oxidation reduction reactions and behave as materials which are on the borderline between battery and EDLC, i.e., pseudocapacitive materials, which are differentiated by the occurrence of redox peaks in CV (cyclic voltammetry) and redox plateaus in galvanostatic CD curves. Although the size reduction cannot considerably alter the CV and GCD profiles for some other battery electrode materials, however, their kinetics are completely different from that in bulk. Some of the transition metal oxides such as molybdenum oxide (MoO_3), iron oxides, and ruthenium oxide (RuO_2), have been used for years as pseudocapacitive materials. These materials consistently exhibit somewhat rectangular cyclic voltammetry profiles and partially linear GCD curves in a variety of electrolytes and charging rates, which contrasts sharply with the electrochemical characteristics of rechargeable batteries.

Among various materials, multiple transition metal oxides such as NiCo_2O_4 [14-16], ZnCo_2O_4 [17, 18], MnCo_2O_4 [19-21], NiMn_2O_4 [22, 23], LiMn_2O_4 [24, 25], MnFe_2Ce_4 [26], and NiZn_2O_4 [27] have been given tremendous importance because of their high specific capacity, accessible oxidation states, the lower activation energy for redox reactions, and good reversible capacities [28-30].

1.10 Molybdates

Recently, metal molybdates have been immensely investigated for electrochemical energy storing systems due to their benign nature, natural abundance, and cost effectiveness [31, 32]. Although, various metal molybdates like NiMoO₄ [33], CoMoO₄ [34, 35], ZnMoO₄ [36-38], CuMoO₄ [39, 40], and MnMoO₄ [41, 42] have shown good electrochemical properties.

1.11 Aims And Objectives

Surface-Controlled ion adsorption-based charge storage mechanisms are one of the reason behind low energy density. Transition metal oxides increase the energy density by providing fast reactions. Thus the objective of this research includes the synthesis of nickel doped molybdates by highly efficient, simple and cost-effective synthetic route, confirming the synthesis by cauterization techniques, and then evaluation of the properties for the supercapacitor application.

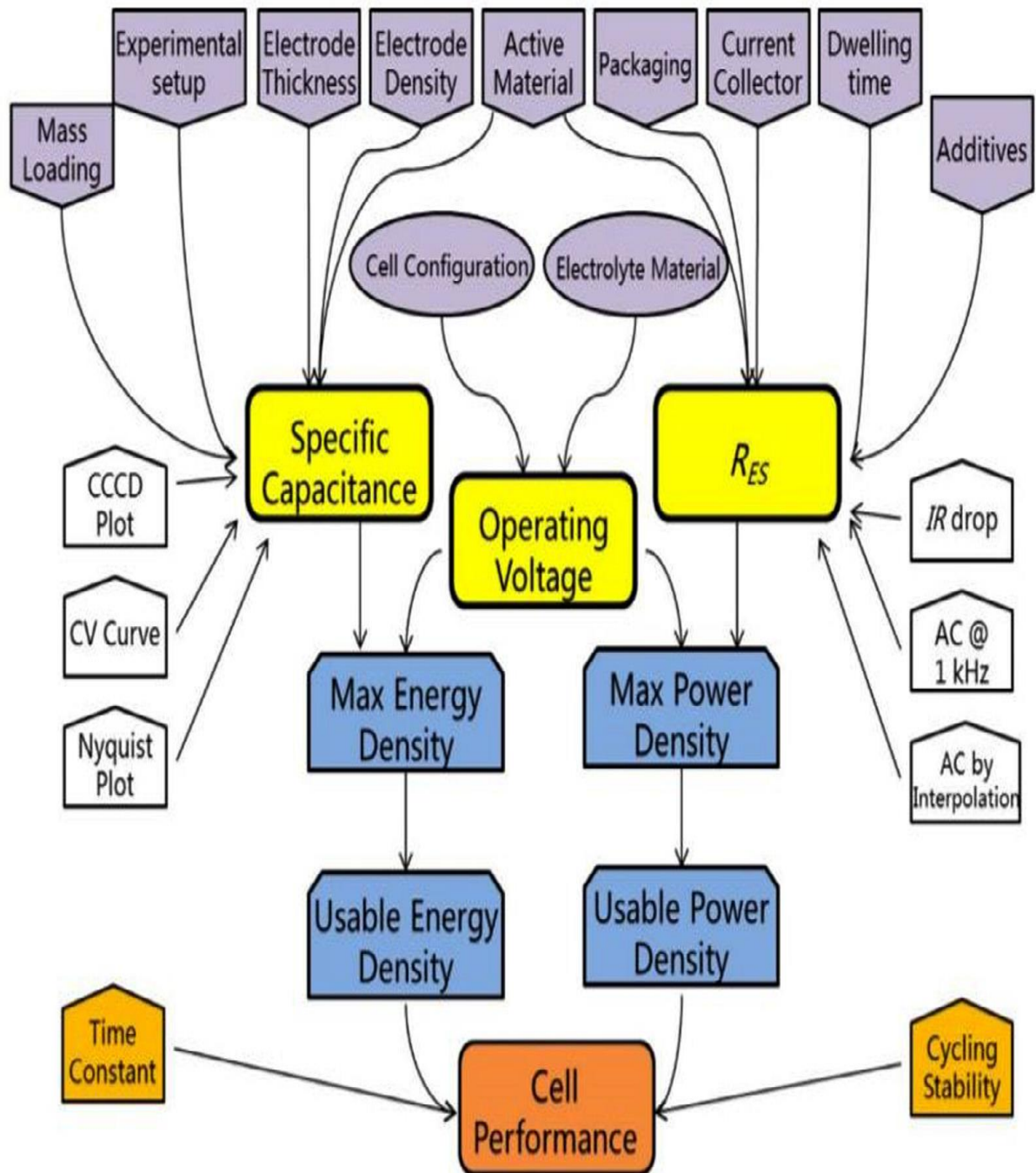


Figure 1.5. Major factors affecting the performance of supercapacitor [43]

CHAPTER 2: LITERATURE REVIEW

[44] A supercapacitor that is asymmetric is designed by using cobalt molybdate (CoMoO_4) as anode and rGO as a cathode. CoMoO_4 synthesized by the sonochemical method and rGO by the hydrothermal method was characterized by Raman, XRD, FTIR, and electrochemical efficiency by the conventional three-electrode system in 1M NaOH. CoMoO_4 and rGO exhibited a capacitance of 98.34 F/g and 168 F/g, respectively. The asymmetric supercapacitor delivered a capacitance of 23.1 F/g and an energy density of 8.17 W h kg⁻¹ at 0.5 mA/cm². Capacitive retention of 85% for 4000 cycles was exhibited by the rGO || CoMoO_4 ASC device.

[45] In this work, cobalt molybdate electro-catalyst is synthesized as an electrode material for supercapacitor by a microwave combustion method using a domestic microwave oven (2450 MHz) at 1000W for 7 minutes. The electrochemical performance of the material is measured by performing different tests. CV profiles demonstrated a pair of redox peaks showing pseudocapacitive type of behavior. Calculated from CV data, the substance delivered a value of 197 F/g at 5mA/cm². However, the highest value of C_s was calculated from GCD data is 133 F/g at 2mA/cm². The material demonstrated 100% retention and R_s value of 1.8 Ω .

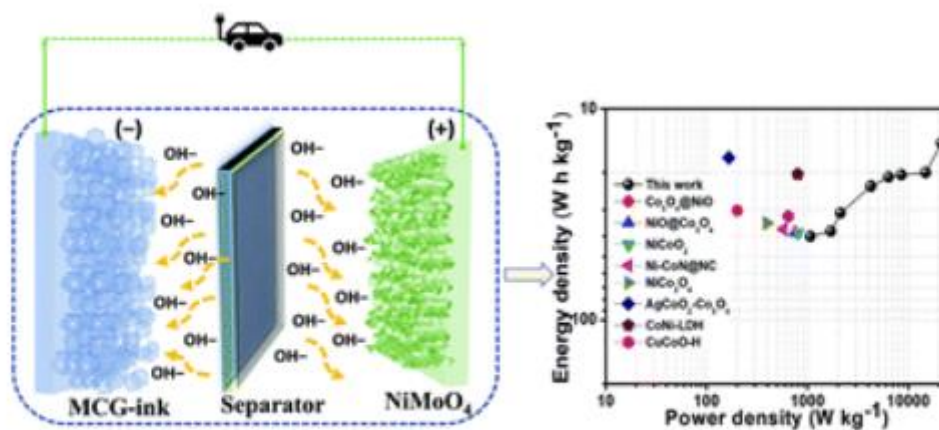


Figure 2.1 Ragone plot and fabrication style

[46] A novel technique is reported for the synthesis of zinc molybdate ($Zn_5 MoO_2 O_{11.5}H_2O$) nano-flowers by magnetic stirring of zinc molybdate ($ZnMoO_4$) nanoparticles in different concentrations of $NaBH_4$ solution to optimize nano-flowers with maximum electrochemical activity. A supercapacitor electrode is then fabricated on Ni foil by using synthesized material, binder, and conducting carbon in a ratio of (7:1:1). The electrode is then tested by performing CV, GCD, and EIS in 3M KOH using three-electrode system. The compared CV and GCD results indicated that the synthesized nano-flowers exhibited good specific capacitance than nanoparticles used as precursor. Moreover, the nano-flowers synthesized in 0.5M $NaBH_4$ manifested highest specific capacitance of 347.5 F/g at current density of 1 A/g. The values of constant b are calculated from the CV profiles which indicated that capacitance originated from both capacitive contribution and diffusion controlled. Calculation of kinetic constants K1 and K2 is done which quantitatively estimated both contributions. Moreover, Wu Zhang et al. noted that material become activated after many cycles, showing an increase in specific capacitance with cycles. The asymmetric capacitor device exhibited 84.5% retention after 5800 number of cycles, C_s value of 84.3 F/g, 26.7 Whkg⁻¹, and 750 Wkg⁻¹.

[47] The flower morphology bismuth molybdate hollow microspheres with a diameter of 1-2 micro-meter was synthesized hydrothermally at 160 C for 16 h. The electrode was prepared by drop-casting on nickel

grid. The material shows C_s of 182 F/g at 1 A/g and retained 95% of the C_s after 400 number of cycles and 80% after 3000 cycles.

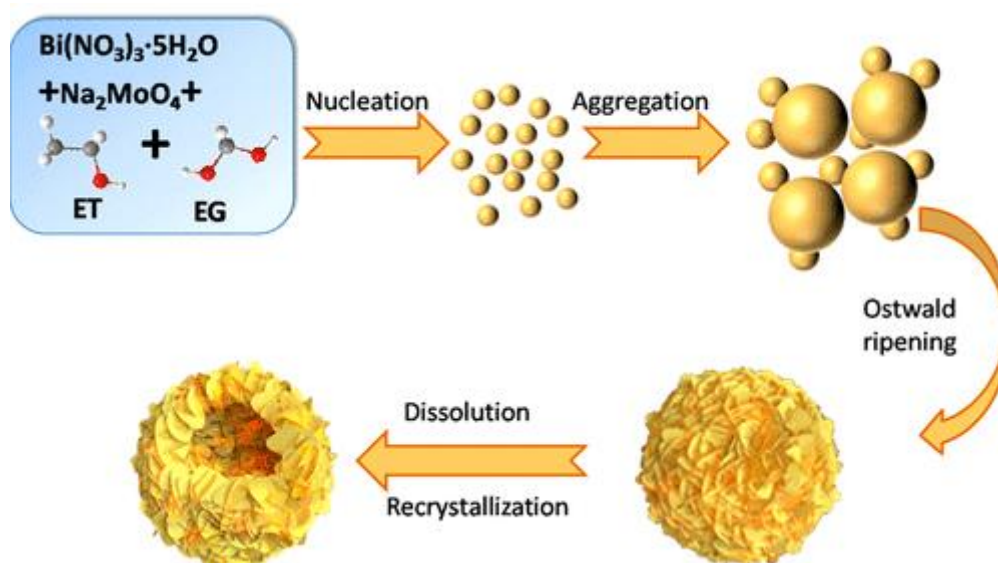


Figure 2.2 Synthetic scheme

[48] A novel flexible device was fabricated by depositing very thin layer of copper stanate nanoparticles on Ni foam. The prepared copper stanate nanoparticles were used as an effective material for supercapacitor's electrode in 2M KOH electrolyte. Cu_2SnO_4 nanoparticles showed a high value of C_s of 2329.68 Fg^{-1} at 1 Ag^{-1} , rate capability of 1330 Fg^{-1} at 70 Ag^{-1} , 81.4% retention of capacitance after 2000 number of cycles at 20 Ag^{-1} and 99.2% columbic efficiency. Asymmetric supercapacitor device comprised of cathode made up of copper stanate and activated carbon anode displayed energy density of 91.04 Whkg^{-1} and 4.35 KWkg^{-1} of power density.

[49] Polypyrrole-iron oxide nanocomposites was synthesized using one step hydrothermal method. Synthesis was performed at four different temperatures to explore the effect of temperature on the properties of material. The nanocomposites exhibited value of C_s of 560 Fg^{-1} at 5 Ag^{-1} with 97.3% retention after 20,000 number of cycles at 40 Ag^{-1} . The nanocomposites synthesized at 180°C exhibited best electrochemical properties. Moreover, it was observed that the concentration of polypyrrole deposited on the nanocoral surfaces was easily controllable by tuning reaction temperature.

[50] Ti-Mo-Ni-O nanoparticle was synthesized by rapid anodization using a foil of titanium molybdenum nickel oxide as a working electrode and foil of platinum as counter electrode at 20V in 0.1M HClO₄. The electrodes were fabricated by drop casting the slurry containing 80:10:10 wt ratio of Ti-Mo-Ni-O nanoparticles, conducting carbon, and binder in DMF solvent. The Ti-Mo-Ni-O delivered a C_s value of 255Fg⁻¹ at 5mVs⁻¹. An asymmetric device showed 68.47Whkg⁻¹ of specific energy and 2058Wkg⁻¹ of power density, 94.6% capacitance retention, and 100% columbic efficiency. The mechanism of charge storage was investigated by Randles-Savick and Transitti methods showing 89.1% of pseudo capacitance and 10.9% of EDLC.

[51] Two dimensional Bi₂MoO₄ nanosheets were synthesized hydrothermally on Ni foam. Powder form of Bi₂MoO₄ was employed as ethanol sensor while nanosheets were employed for supercapacitor applications in 1 molar KOH aqueous solution. Nanosheets exhibited C_s of 655.5 mF/cm² at a current density of 1mA/cm² with energy density of 22.76 x 10³ Wh/cm² and a power density of 347.8 x 10³ W/cm². When Bi₂MoO₄ was employed as sensor, a good response of 92% for 150 ppm ethanol was noted at 300° C.

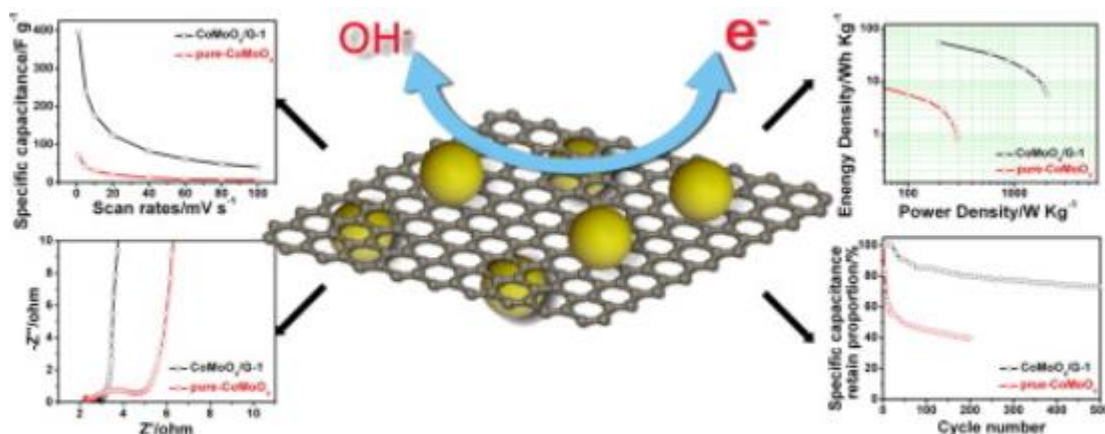


Figure 2.3 structure and working of molybdate

[52] Mn₂SnO₄ nanocube particles were synthesized by using sonochemical synthesis technique. The as synthesized nanocubes were evaluated by making an electrode by pasting the electrode slurry which is comprised of 75 wt% Mn₂SnO₄ as active material, 20 wt% conducting carbon and 5 wt% binder in solvent

NMP. A conventional three electrode system was used for measurement of electrochemical properties in 3M KCL as an electrolyte. A potential window of 0 to 1V was used for working electrode while for symmetrical supercapacitor, a potential window of 0 to 2V was used. The material exhibited a maximum C_s of 298 F/g, C_s retention of 82% after 4000 number of cycles. While symmetrical supercapacitor delivered an E value of 30.4 Wh/kg at a P value of 1.58 W/kg.

[53] $ZnMn_2O_4$ nanoparticles were synthesized by cost-effective and efficient urea combustion technique. The prepared nanoparticles were then characterized by FESEM, TEM, XRD, and an area analyser. $ZnMn_2O_4$ nanoparticles were found out to be mesoporous and crystalline in nature. The electrochemical properties of the prepared nanoparticles were checked by performing GCD, CV and EIS in 3 molar LiOH electrolyte. The C_s which was calculated from CV data was 160 F/g. The particles exhibited 100% coulombic efficiency and good cyclic stability for 5000 cycles. It was observed that the improved electrochemical properties of the synthesized nanoparticles was ascribed to the homogenous distribution of pores of the size 10-30 nm.

[54] A porous ternary nanohybrid was synthesized from $NiMn_2O_4$, polyaniline, and reduced graphene oxide. $NiMn_2O_4$ was synthesized hydrothermally at 180°C for 6h and the obtained product was annealed at 450 °C for 2h. Polymerizing of aniline in the presence of rGO and $NiMn_2O_4$ give rise to ternary composite. The electrode was fabricated by drop-casting the electrode ink on Ni foam. The slurry was prepared in NMP solvent by dissolving 60% of the active material, 20% PTE binder and 20% carbon black. CV and GCD was performed in the voltage window of -0.2V to 1V by means of three-electrode system. The synthesized ternary nanohybrid exhibited the C_s of 757 F/g while pristine $NiMn_2O_4$ exhibited 194 F/g and a binary composite of rGO and $NiMn_2O_4$ exhibited the C_s of 436 F/g. The ternary nanohybrid delivered an E value of 70Wh/kg and 83% capacitive retention after 2000 number of cycles. The good super-capacitive behaviour was ascribed to the wrapping of conductive polymer on rGO and $NiMn_2O_4$.

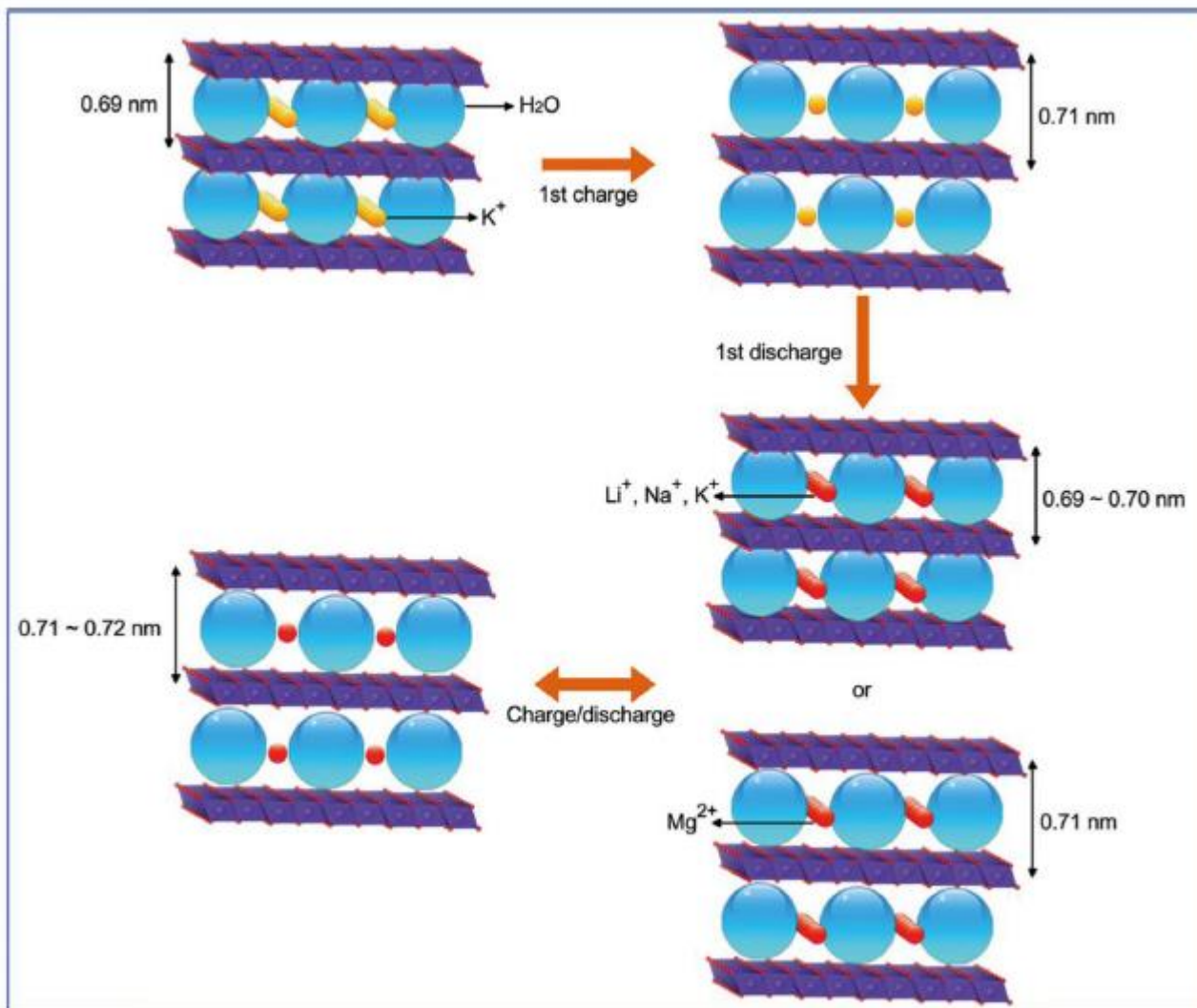


Figure 2.4 Charging and discharging by intercalation

[55] In this study, simple hydrothermal procedures were used to create NiMoO₄ nano-rods and nano-spheres. The hierarchical structure based NiMoO₄ nano-rods had a diameter of around 1.5 μm and were made of 15–25 nm thick nanosheets which were mesoporous in nature. The NiMoO₄ nano-spheres had dimensions of 90 nanometres diameter and 250 nanometres to 1 μm of length. For usage as supercapacitor's electrode material, their electrochemical characteristics were examined. The flexibility and excellent conductivity of the NiMoO₄ nano-spheres were credited for their larger capacitance, amazing rate capability, and good cycling stability. Varying current densities from 1 to 10 A/g, the C_s were 970, 925.8, 885.5, 899.1, and 871.4 F/g, respectively. Amazingly, at a P value of 2000 W/kg, the E value was able to reach 15.1 Wh/kg. The

NiMoO₄ nano-spheres continued to exhibit a high C_s of about 625.7 F/g at a current density of 5 A/g after 2500 number of cycles. The hierarchical NiMoO₄ nano-spheres may be a best material for usage as good-performance supercapacitors according to these data.

[56] One of the growing energy sources for powering the electronic devices we use every day is the supercapacitor. Although many different types of supercapacitors have been developed and shown, their market potential could increase if the electrode is given access to other physicochemical properties, such as optical properties. Here, we propose an electrochromic supercapacitor built on a thin nickel molybdate nanoflakes that was created using the quick and precise SILAR method. The polycrystalline nanoflakes NiMoO₄ electrode has an area of approximately 86.3 cm² that is very electrochemically active. One of the growing energy sources for sustaining the electronics that we use every day is the supercapacitor. Although many different types of supercapacitors have been developed and shown, their market potential could increase if the electrode is given access to other physical characteristics, such as optical properties. Here, we propose an electro-chromic supercapacitor built on a small NiMoO₄ nano-flake film that was created using the quick SILAR method. The nano-flake nickel molybdate nanoparticles have an integrated area of approximately 96.3 cm² that is very electrochemically active. Ion incorporation and de-intercalation are made simple by the nano-porous design of the material. The charged state of the nano-flake NiMoO₄ electrode is brown, while the discharged state has a strong optical fluctuation of 66% and is clear. The electrode exhibits an excellent colouring efficiency of 21.34 cm²/C and a C_s of 1852 Fg⁻¹ at a scan rate of 1 Ag⁻¹. When the electrode gets charged at various potentials, dynamic graphical information that represents the amount of stored energy in the device is received. After 2600 charge-discharge cycles, the device still has sixty-five percent of its original capacity. The outstanding performance of the effective supercapacitor made from nano-porous NiMoO₄ is credited to the simultaneous effect of the integrated area of the nano-porous morphology that is electro-chemically active.

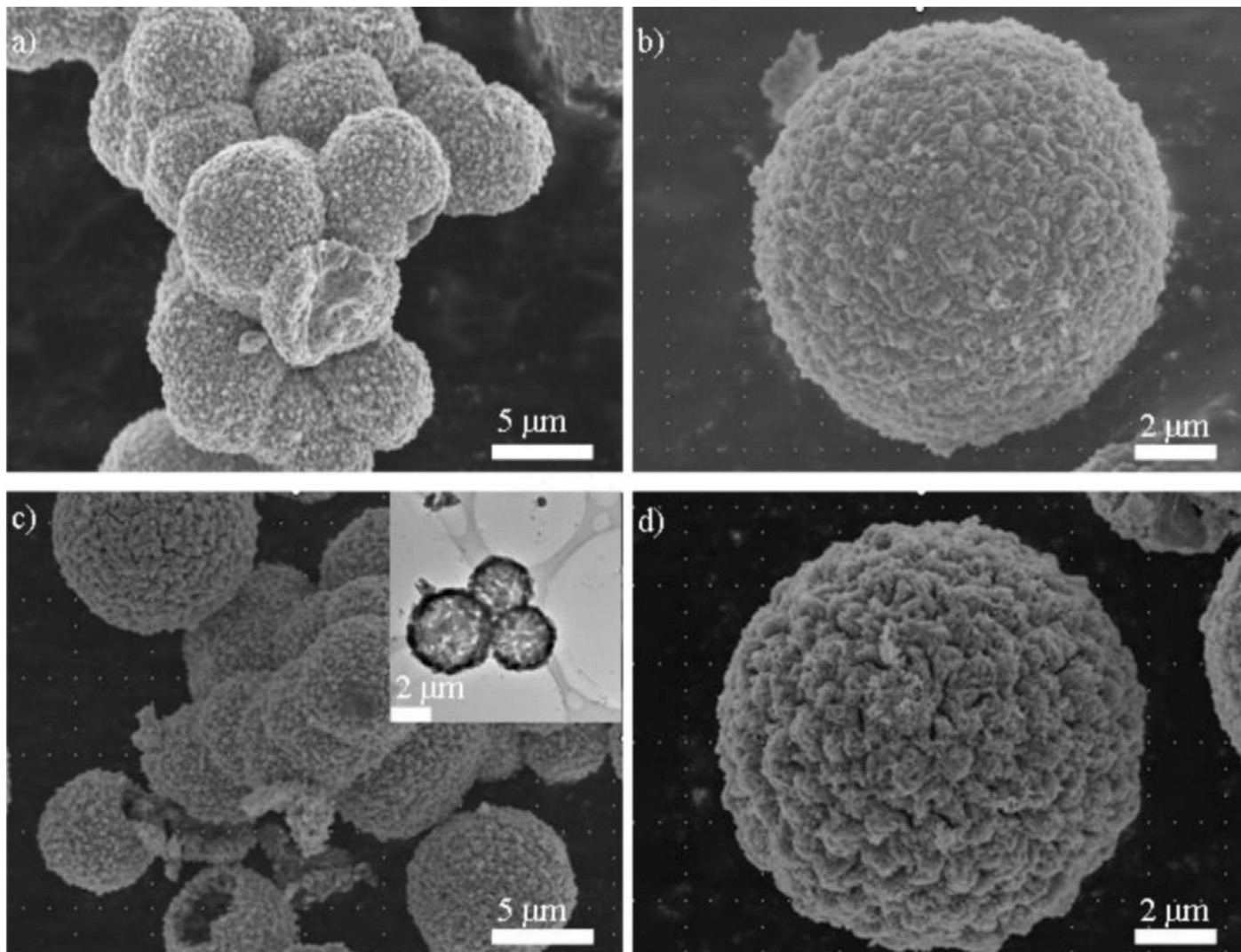


Figure 2.5 Spherical morphology of nickel molybdate

[57] The $\text{MgMoO}_4/\text{MgWO}_4$ nanocomposites are made using a poly-acrylamide gel technique and low temperature annealing technology. To create a unique hetero-junction arrangement with (210) and (110) crystal planes MgWO_4 and MgMoO_4 were linked. Magnesium molybdate and magnesium vanadate heterojunction nanocomposite elevated the amount of adsorbed oxygen in the system but were unable to change the band gap value. The capacitance of MgMoO_4 with 20 wt% of MgWO_4 nanocomposites is 225 mA h g^{-1} , according to an electrochemical performance investigation. The $\text{MgMoO}_4/\text{MgWO}_4$ heterojunction nanocomposites manufacturing process, composition based on elements of the carriers have a good effect on the supercapacitor performance. Due to the complementary relationship between the

concentration of oxygen which get absorbed and the speed of charge carrier replication, photoluminescence research demonstrates that the nanocomposites display a higher peak than pristine at 528 nanometres.

[58] One of the greatest potential energy storage technologies is the supercapacitor, and its efficiency is dependent on the design and make-up of the materials used for the electrodes. Metal oxides are a promising source of electrode material; however they suffer from poor conductivity and inadequate stability during cycles in the context of the application. As a result, numerous research fields are focused on creating novel material composites incorporating nanostructures to address this issue. In the present investigation, a straightforward hydrothermal process is used to effectively load MgMoO_4 onto flower shaped CuCo_2O_4 formed on the nickel foam as a substrate. Its general efficiency can be improved by this unique composite structure's ability to work in synergy with both of its components. The findings demonstrate that the electrode material has the best chemical and physical structure among other composite components, as evidenced by its significant capacitance of 1155 F/g at one A/g. The asymmetrical supercapacitor device also has an E value of 26.8 Wh/kg at a power value of 165 W/kg and outstanding cyclic stability (82.5% is still present after 10,000 number of cycles). According to the aforementioned findings, the produced material for electrodes has outstanding possibilities as supercapacitor materials for electrodes.

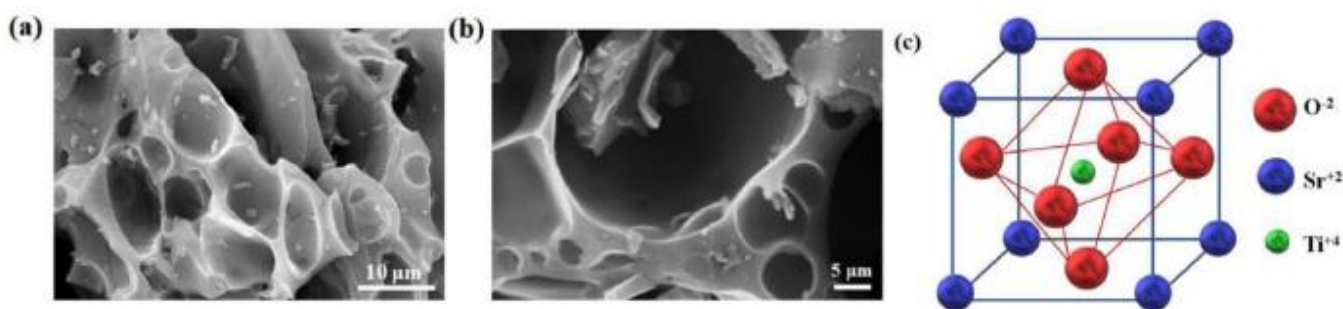


Figure 2.5 Porous morphology

[59] For the initial time in history, the use of microwaves is used to create simple and effective reduced graphene oxide-cobalt molybdate nanocomposites. By in situ reduction, CoMoO_4 nanoparticles which are strongly affirmed to graphene sheets are created as the end product's nanocomposites. By using FTIR (Fourier-transform infrared spectroscopy), Raman spectroscopy, (XRD) X-ray diffraction, thermo-

gravimetric analysis, (XPS) X-ray photoelectron spectroscopy, and SEM (scanning electron microscopy, the produced RGO/CoMoO₄ nanocomposites have been comprehensively characterised. The produced nanocomposites, which is significant, provide excellent electrochemical properties for super capacitors. Compared to pure cobalt molybdate and a composite of reduced graphene oxide/cobalt molybdate, the results demonstrate that RGO/CoMoO₄ nanocomposites have significantly improved electrochemical capabilities. A specific capacitance of about 225 F g⁻¹ was attained by RGO/CoMoO₄ nanocomposites with a 27.4 wt% CoMoO₄ content. This capacitance was estimated from the CV graphs at five mV s⁻¹. The mutually beneficial relationships between the different components are responsible for effective electrochemical activity.

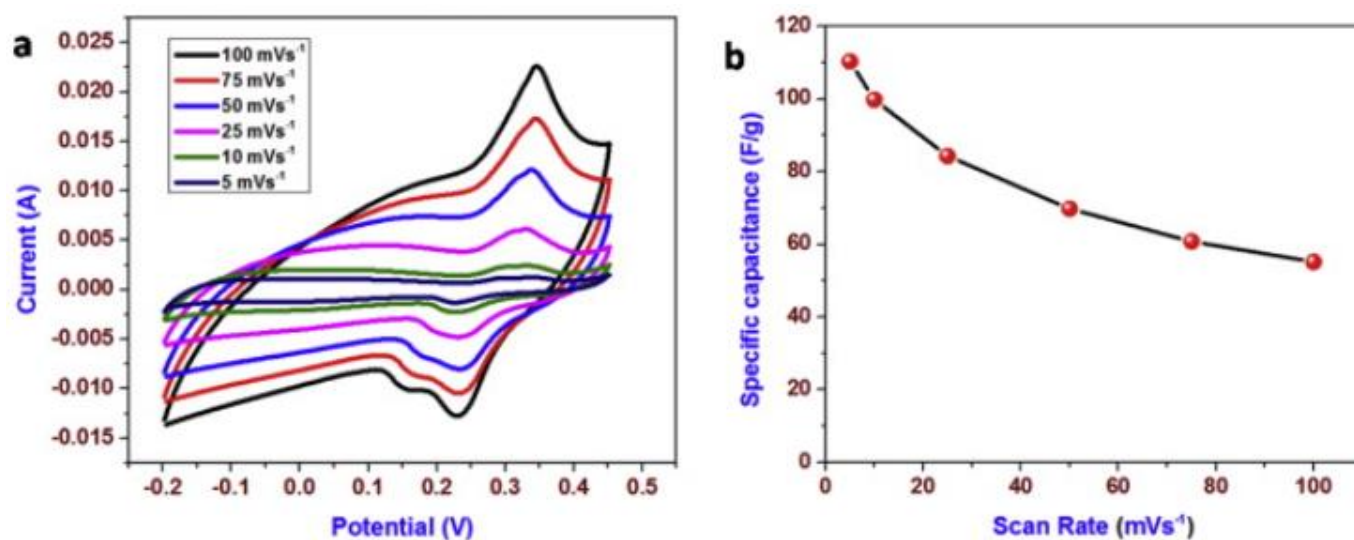


Figure 2.6 Cyclic voltammetry profile

[35]The CoMoO₄/graphene with better electrochemical characteristics for supercapacitors was easily synthesized using a hydrothermal technique. After adding ammonium hepta molybdate and changing the pH level, the ions became absorbed on the GO surface. Following a hydrothermal reaction, CoMoO₄ particles were produced on the graphene sheet. Large electrically charged areas and high surface-to-body ratios in the in their original form CoMoO₄/G composites allowed for quick charge transfer and simple access to OH ions. By using the curve of the CV at a voltage of 1 mV s⁻¹, CoMoO₄/G hybrids were able to attain C_s of approximately 304.5 F g⁻¹ and an E value of about 5445.8 Wh/kg. Additionally, the CoMoO₄/G materials

showed reduced electrochemical resistance. This is excellent cycling capability, and a long cycle life in compared to pure CoMoO₄.

[60] Three various weight proportions of graphene were used in a novel and economically advantageous hydrothermal process to create hexahedral morphology of MnMoO₄ and its hybrid composite with graphene. Analytical methods like XRD, FTIR examinations and Raman were used to figure out the material's phase and composition. The MnMoO₄ and MnMoO₄/graphene compositions with the largest specific capacitances that at 2 A g⁻¹ and 228 F g⁻¹, respectively, were electrochemically characterized as pseudocapacitive substances in 1 molar Na₂SO₄. The produced substances behaved to an extensive range of operating voltages from (-)1 V to (+)1 V, contrasting many other pseudocapacitive materials for electrodes, which in turn led to an elevated density of energy while suffering significantly from a decrease in power density. At an identical supply rate of 3000 W/kg, 128 Wh/kg and 132.2 Wh/kg were attained by the manganese molybdate/graphene oxide composite and manganese molybdate composite, respectively. After thousand continuous CCD cycles at an unchanged current density of 8 A g⁻¹, the combined impact of graphene and the pseudocapacitive MnMoO₄ resulted in raised stability during cycles with an individual capacitance preservation of 89%, which was considerably greater than the MnMoO₄'s 74 percent.

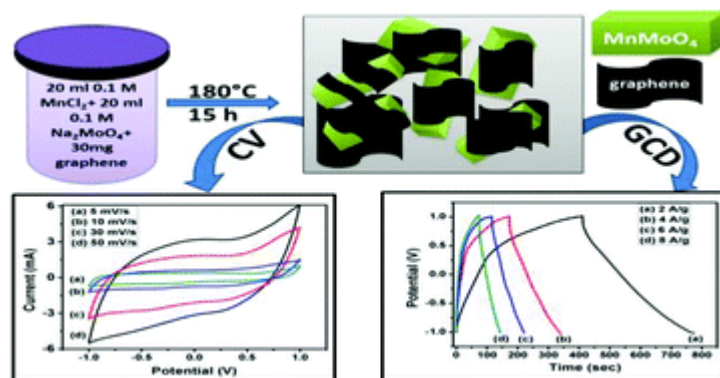


Figure 2.7 Graphical abstract

CHAPTER 4: MATERIALS AND METHODS

3.1 Materials

All chemicals were of analytical grade and used without any additional treatment. Chromium (II) Nitrate hexahydrate ($\text{Cr}(\text{NO}_3)_2 \cdot 6\text{H}_2\text{O}$, purity 99+%), Hexammonium heptamolybdate tetrahydrate ($(\text{NH}_4)_6\text{Mo}_7\text{O}_{24} \cdot 4\text{H}_2\text{O}$, purity 99+%), Nickel (II) Nitrate hexahydrate ($\text{Ni}(\text{NO}_3)_2 \cdot 6\text{H}_2\text{O}$, purity 99+%), nafion ($\text{C}_7\text{HF}_{13}\text{O}_5\text{S} \cdot \text{C}_2\text{F}_4$, purity 99+%), ethanol ($\text{C}_2\text{H}_6\text{O}$, purity 99+%), potassium hydroxide (KOH, purity 99+%), and sodium hydroxide (NaOH, purity 99+%) were purchased from Sinopharm Chemical Reagent Co., Ltd, China.

3.2 Synthesis

All five samples $\text{Ni}_x\text{Cr}_{2-x}(\text{MoO}_4)_3$ ($x=0, 0.05, 0.10, 0.15,$ and 0.20) were prepared by the co-precipitation method followed by an annealing process. $\text{Cr}_2(\text{MoO}_4)_3$ was prepared by separately dissolving 5mmol of $\text{Cr}(\text{NO}_3)_2 \cdot 6\text{H}_2\text{O}$ and 5mmol of $(\text{NH}_4)_6\text{Mo}_7\text{O}_{24} \cdot 4\text{H}_2\text{O}$ in beakers each containing 30ml of DI water followed by stirring at 50°C , thus making solutions A and B, respectively. To maintain a pH of 10, 26.1 mmol of NaOH was added to solution B. Two solutions were mixed and stirred for 2 hours at 60°C . The precipitates were centrifuged at 8000 rpm, washed several times with DI water and absolute ethanol, and then dried overnight in a vacuum oven at 60°C . The final product was obtained after annealing in air at 700°C for 2 hours.

The $\text{Ni}_x\text{Cr}_{2-x}(\text{MoO}_4)_3$ ($x=0.05, 0.10, 0.15$ and 0.20) were synthesized by making three solutions A, B, and C in 15 ml DI water, containing calculated amounts of $\text{Cr}(\text{NO}_3)_2 \cdot 6\text{H}_2\text{O}$, $(\text{NH}_4)_6\text{Mo}_7\text{O}_{24} \cdot 4\text{H}_2\text{O}$ and 26.1 mmol of NaOH, and $\text{Ni}(\text{NO}_3)_2 \cdot 6\text{H}_2\text{O}$, respectively. Solutions A and C are mixed in Solution B under stirring for 2

hours at 60°C. The final products were obtained by following the same procedure as discussed for Cr₂(MoO₄)₃.

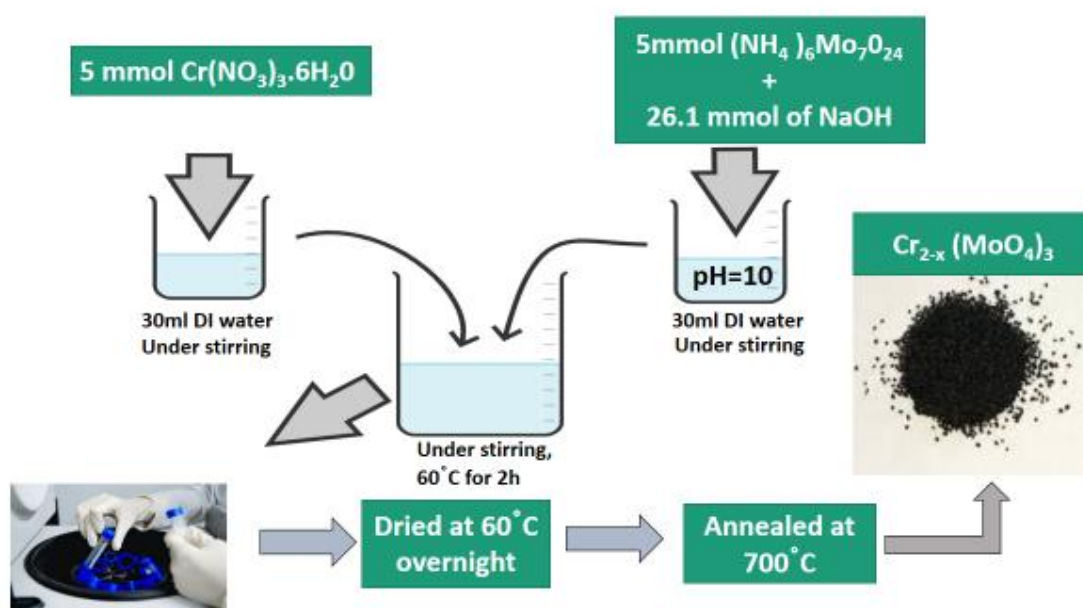


Figure 3.1. Schematic scheme depicting the synthesis of chromium molybdate.

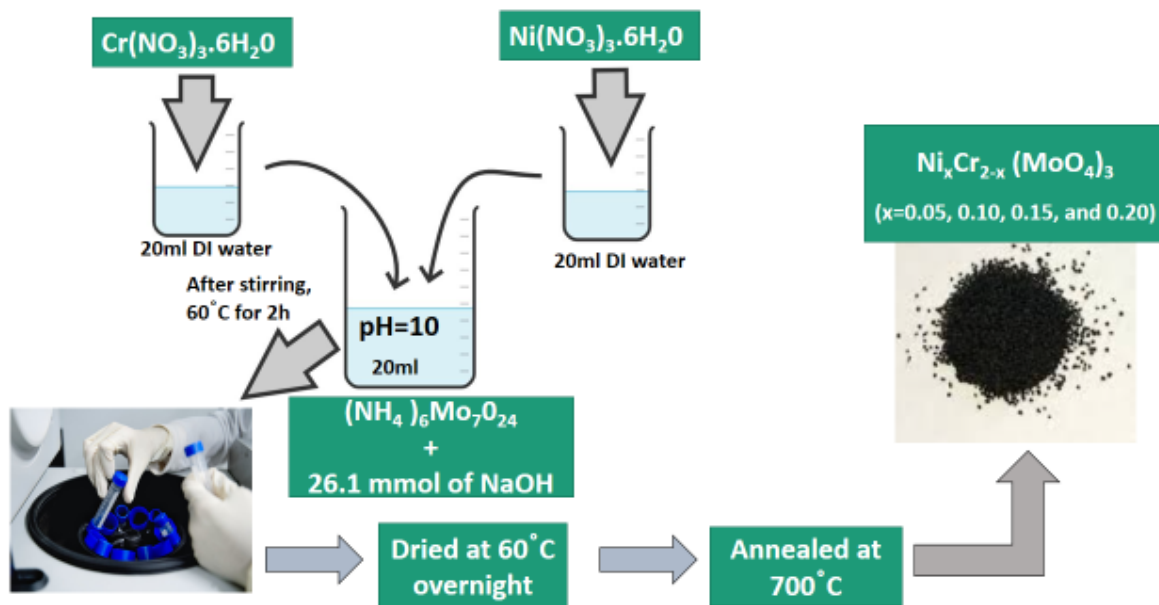


Figure 3.2. Schematic Scheme showing the synthesis of nickel Doped Chromium Molybdates

CHAPTER 4: CHARACTERIZATION

The prepared materials were characterized by different techniques including X-ray diffraction (XRD), Raman spectroscopy, scanning electron microscopy (SEM), and energy dispersive spectroscopy (EDS).

4.1 Introduction to Characterization Techniques

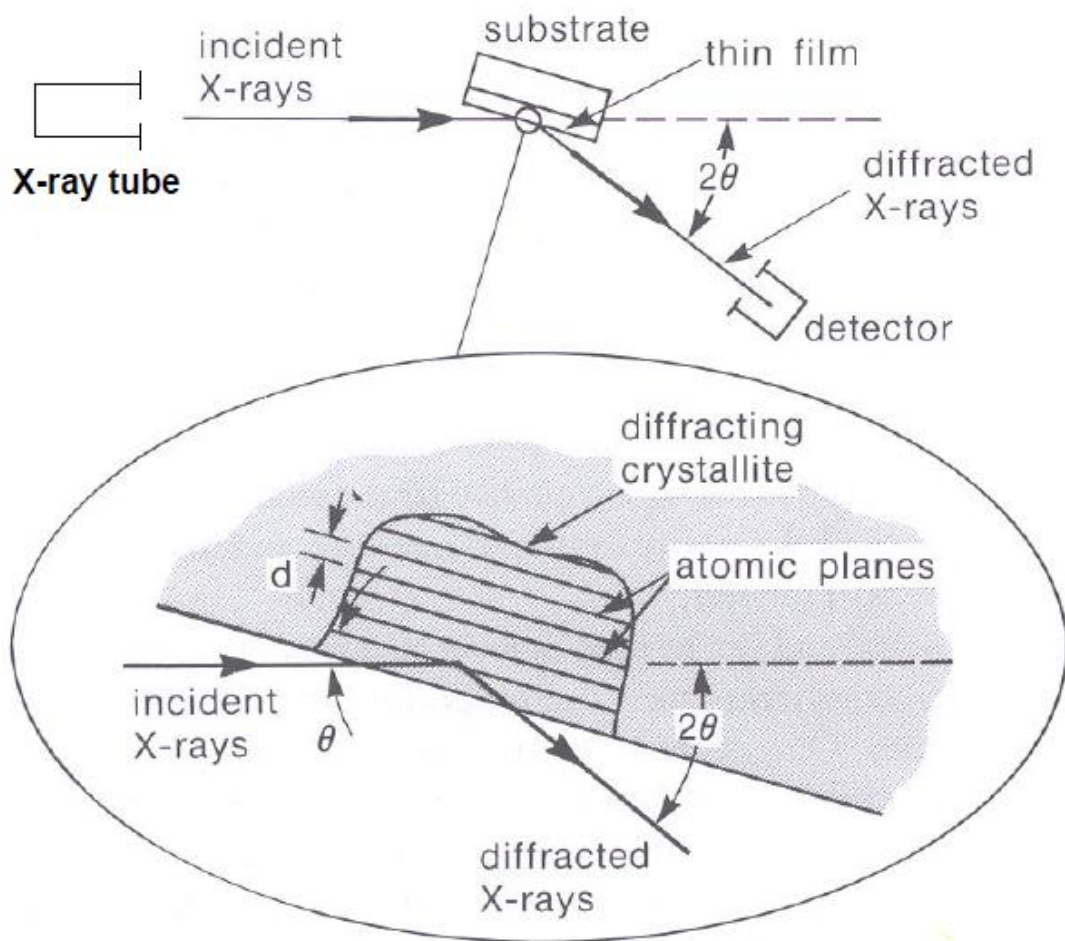
4.1.1 X-ray Diffraction

In 1913, Bragg formed a partnership and explained the reason for the reflection of X-rays from the crystal planes at specific angles which differ from the angles of incidence.

Working of X-Ray diffractometer

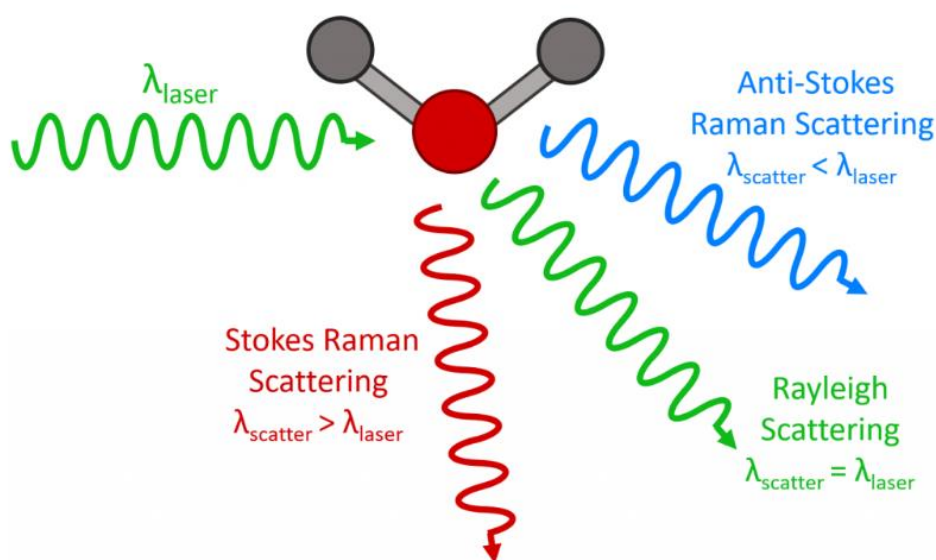
The three main parts of an X-ray diffractometer are an X-ray tube for the production of X-rays, a detector for the reflecting X-rays and a sample holder.

X-rays are produced by igniting the filament at very high temperatures that electrons are knocked out of the materials, then high volts are provided for speeding the knocked-out electrons towards a target. These high-speed electrons then hit the samples or the material under study. Characteristic spectra of X-rays displayed on the screens when high energy containing beam of electrons containing sufficient energy to knock electrons out of the material. K and K parts of these spectra are among their many different elements. K1 and K2 make up a portion of K. K1 is twice as intense as K2, however it has a somewhat shorter wavelength. The target material (Cu, Fe, Mo, and Cr) exhibits properties at certain wavelengths. Monochromatic images must be filtered using foils or crystal monochrometers.

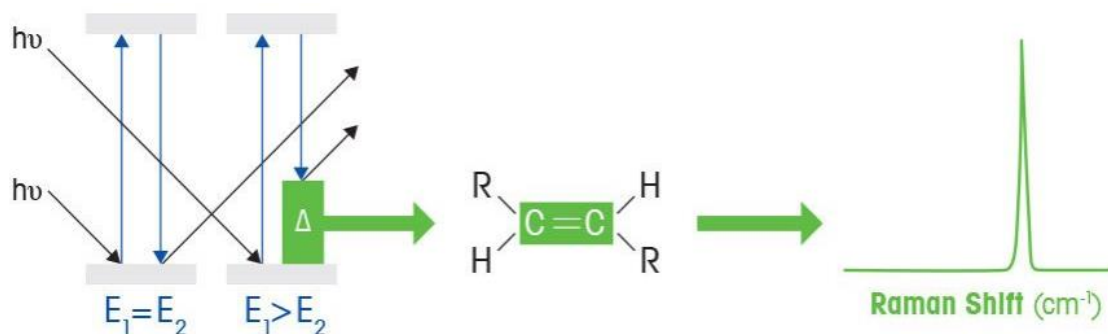


4.1.2 Raman Spectroscopy

An effective method for identifying chemical species is Raman spectroscopy. Raman spectroscopy, like other spectroscopic methods, finds specific interactions of light with matter. This method specifically makes use of Stokes and Anti-Stokes scattering to look at molecular structure. There are various types of scattering that can happen when radiation from the visible or near infrared rays interacts with a molecule.



Usually, the change in wavenumber (cm^{-1}) caused by the incident light source is used to measure this. Stokes Raman scattering is observed in the lower wavenumber region and anti-Stokes Raman scattering in the higher wavenumber region. Raman measurements can be made with sources of any wavelength because they measure the change in wavenumber; however, the near infrared and visible spectrum are typically employed.



4.1.3 Scanning Electron microscopy

A sophisticated analytical instrument that is far superior to conventional light microscopy is scanning electron microscopy (SEM). Using visible light in the 400–700 nm range, the usual array of magnifying lenses in a compound microscope offers sample magnification of up to 1000x. Secondary and backscattered electrons (BSE), as well as x-rays, are produced when electrons strike a surface. These signals, which are indicative of the sample's elemental composition, shape, and crystalline structure, are captured by BSE and x-ray detectors in the chamber.

❖ Secondary Electrons

The electrons which are known as secondary electrons are released from the sample, deep inside of the atomic structure. These electrons are produced due to interactions being inelastic in nature between the electron beam and the sample. These come from within a few nanometres of the sample surface and exhibit lower amount of energy as compared to that of the backscattered electrons. These electrons provide topographic data of the samples as being sensitive to the surface.

❖ Backscattered Electrons

After interactions between the electron rays and the substance, which are inelastic in nature, the backscattered electrons are reflected. They provide information about the composition of the substance.

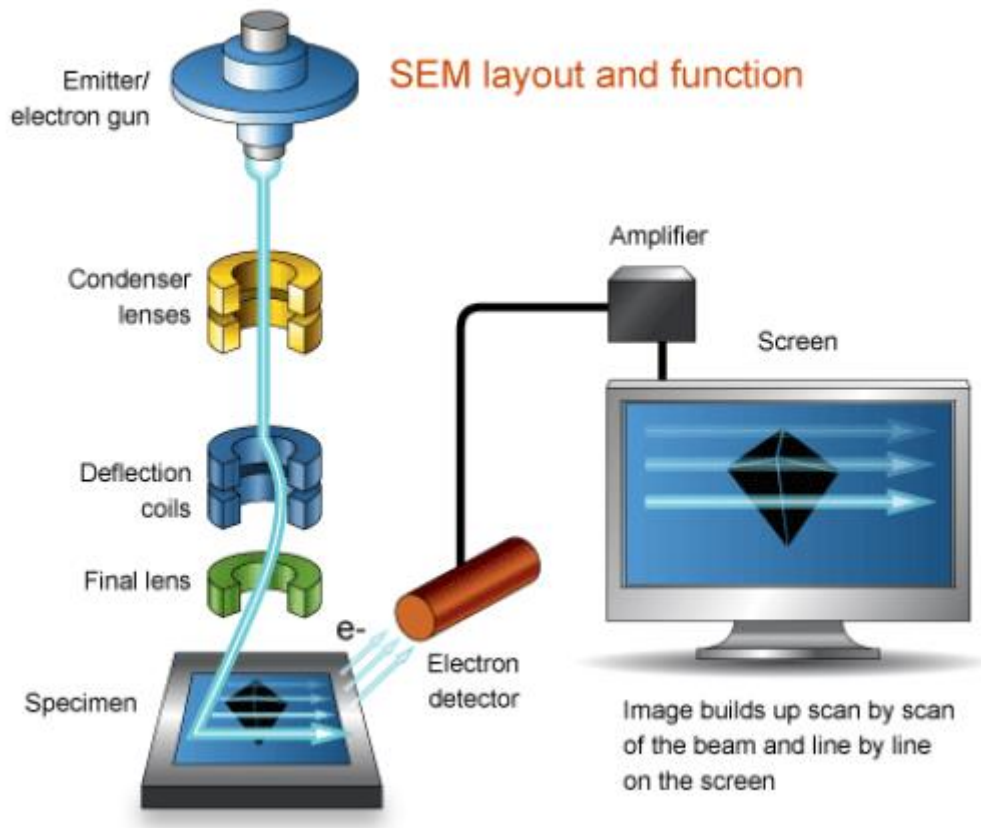
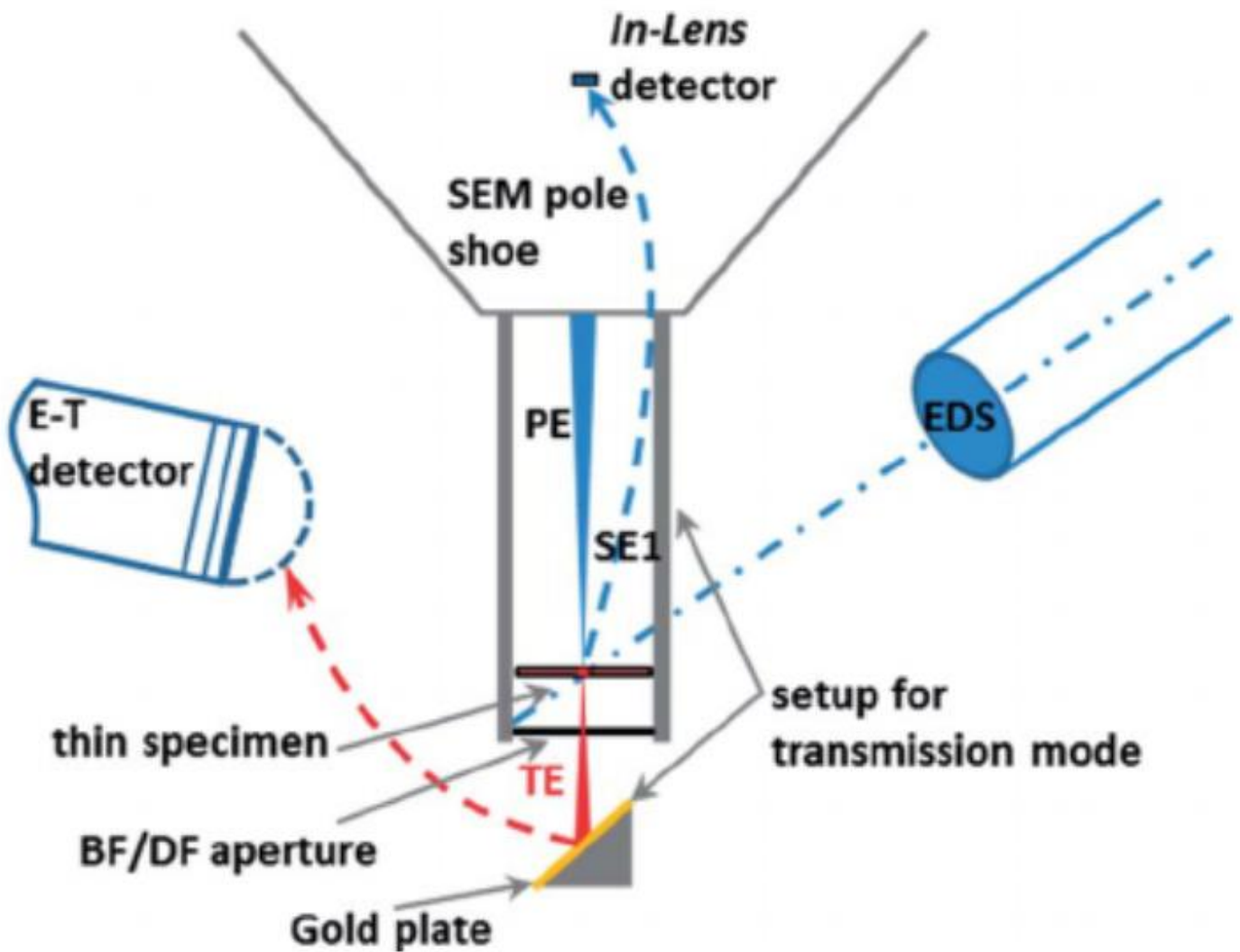


Figure 4.1 Configuration of SEM [61]

4.1.4 Energy dispersive X-rays Spectroscopy (EDS)

EDS or EDX, energy-dispersive X-ray spectroscopy, is an analytical technique which gives information about the elements and the rough estimate of the amount of each detected elements present in the substance under study. The electrons in the target atoms are ejected from their inner shells when a sample is hit with a beam of high-energy electrons, leaving an electron vacancy. In a subsequent transition that produces X-rays, the electrons on the higher levels are moved to the inner levels. Every element in the periodic table has a different electrical set up, which affects its energy level. The resulting X-rays are therefore unique to each element.

The Kev and peak intensity of the EDS data are plotted on an x-y axis in a graph. A computer programme converts the atoms that the energy changes represent at the highest place on the x-axis.



4.2 Electrochemical Evaluation

Electrodes were fabricated by preparing a slurry from active material, acetylene black, and nafion in the weight ratio of 80:10:10 in ethanol. The slurry was drop-casted on the activated nickel foam ($1 \times 1 \text{ cm}^2$) with a few micron thicknesses and then dried overnight at 60°C in a vacuum oven.

The electrochemical properties of the as-prepared electrodes were evaluated on Gamray Electrochemical Workstation at room temperature by the conventional three-electrode system constituting Ag/AgCl, platinum wire, and prepared electrodes as reference, counter, and working electrodes, respectively. Moreover, a 2M

KOH solution was used as an aqueous electrolyte. Cyclic Voltammetry (CV) was performed in the potential window of 0-0.5 V at different scan rates. Galvanostatic charge-discharge (GCD) analyses were conducted at current densities ranging from 1 to 5 A/g. Electrochemical Impedance Spectroscopy (EIS) was carried out at open circuit potential in the frequency range of 0.01-10kHz with an AC voltage perturbation amplitude of 10 mV. Specific capacitance was calculated from CV data and charge-discharge profiles using the following equation (1) and (2), respectively.

$$C_s = \frac{\int IdV}{m \times v \times \Delta V} \quad (1)$$

$$C_s = \frac{I \Delta t}{\Delta V \times m} \quad (2)$$

Where C_s , IdV , m , v , and ΔV in equation (1) stands for specific capacitance (Fg^{-1}), the area under the curve (AV), mass loading of the electrode (g), and voltage drop (V), respectively. While, in equation (2), C_s , I , Δt , ΔV , and m are specific capacitance (Fg^{-1}), discharge current (A), discharge time (s), voltage drop during discharging (V), and mass loading of the electrode (g), respectively. The energy density (E, Whkg^{-1}) and power density (P, kWkg^{-1}) were calculated according to equations (3) and (4), respectively [38]

$$E = \frac{C_s \Delta V^2}{2 \times 3.6} \quad (3)$$

$$P = \frac{3600 E}{\Delta t} \quad (4)$$

Where C_s , Δt , ΔV^2 denote the same meaning as described for equations.

(1 and 2)

CHAPTER 5: RESULTS AND DISCUSSIONS

The morphology of the as-prepared materials is analysed by SEM. High-magnification SEM images of all the materials are shown in Figure 1.1 and low-magnification images are given in the supporting data. Figure 1.1a and Figure S1 display SEM images of material where $x=0$. An irregular nanoflakes-like morphology is observed when nickel concentration is zero. With the incorporation of nickel in $x=0.05$ (as shown in Figure 1.1b and Figure S2), particles started to orient into a more homogenous spherical morphology. Moreover, when the concentration of nickel is increased from $x=0.10$ to $x=0.15$, it is seen that the particles aggregate and take the shape of nanorods., as shown in Figures 1c, 1d, and S3, S4, respectively. However, increasing the nickel dopant to $x=0.20$ (Figure 1.1e and S5), more nanorods separate as individual nanoparticles and it is also observed that the diameter of nanorods has been increased.

The presence of nickel in nickel-doped samples was verified by Energy-dispersive spectroscopy (EDS). The EDS spectra demonstrate the emission peaks match up to Cr, Mo, O, and Ni in all Nickel-doped samples thus showing successful doping of nickel.

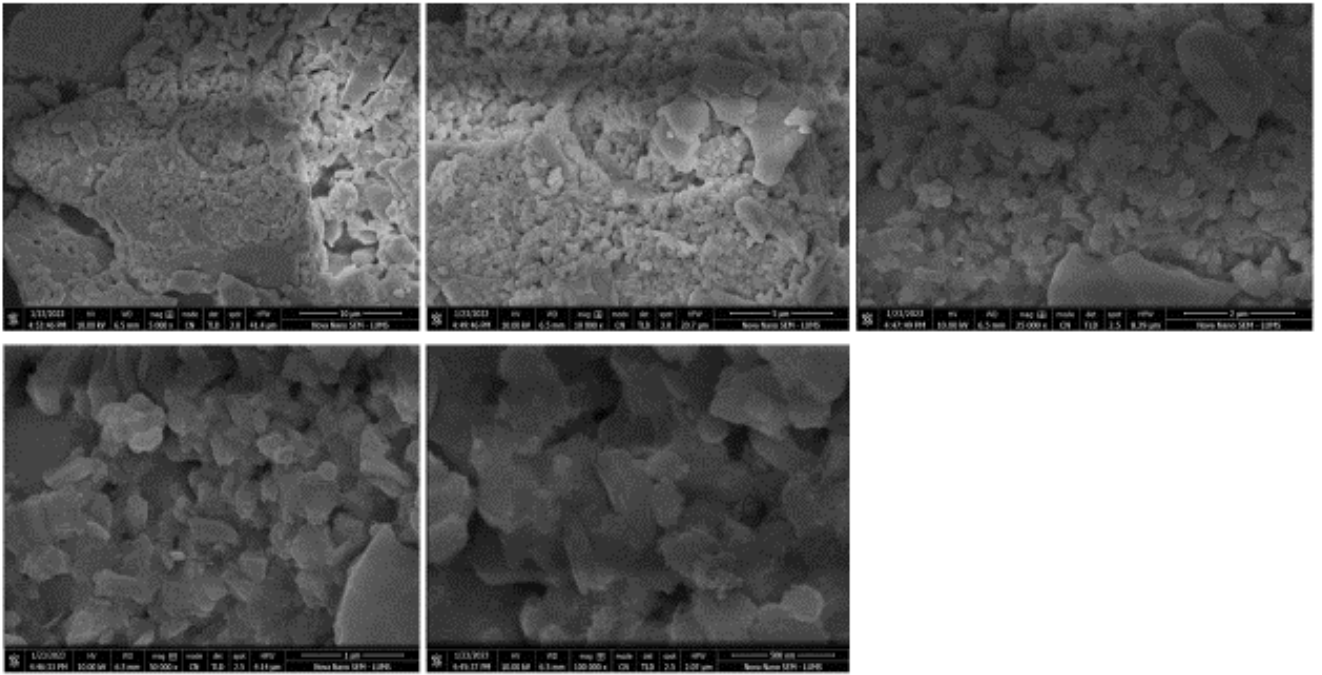


Figure 5.1. SEM images of $x=0$

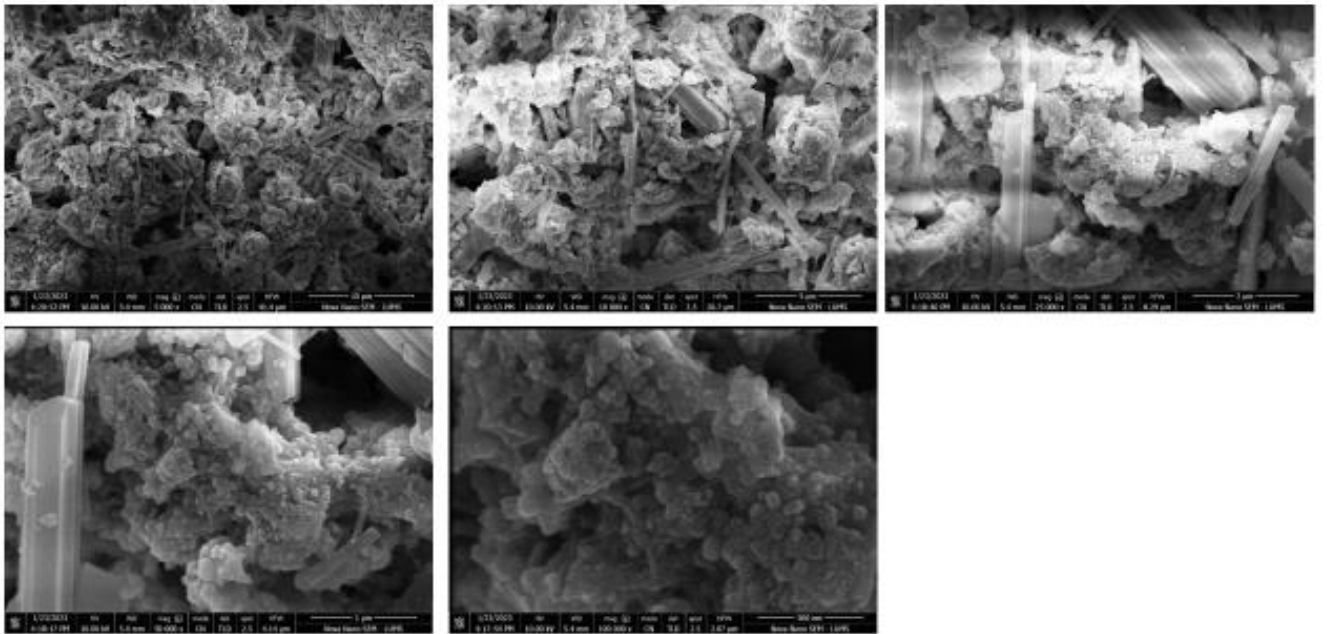


Figure 5.2. SEM images of $x=0.05$

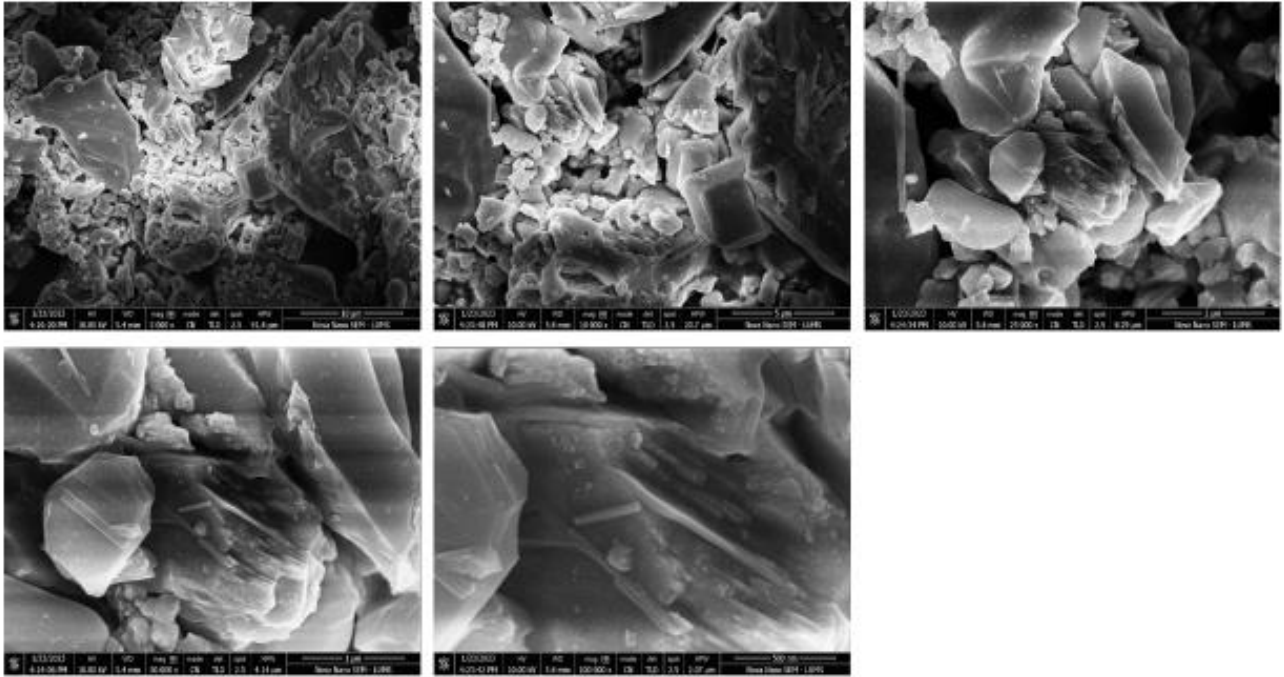


Figure 5.3. SEM images of $x=0.10$

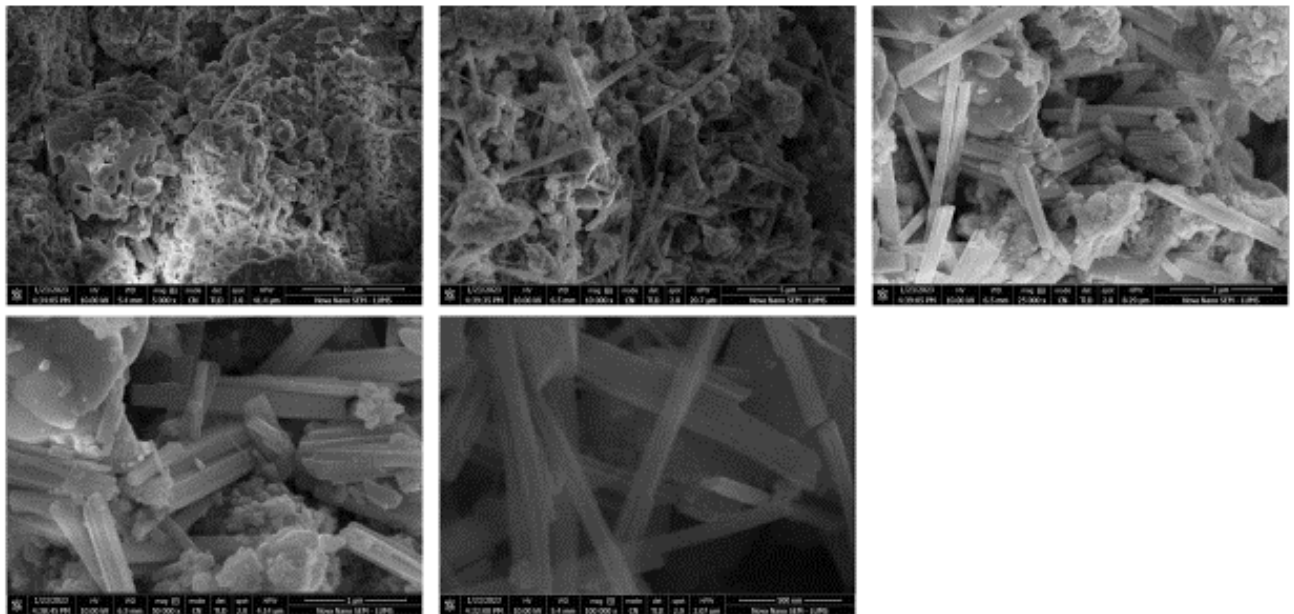


Figure 5.4 SEM images of $x=0.15$

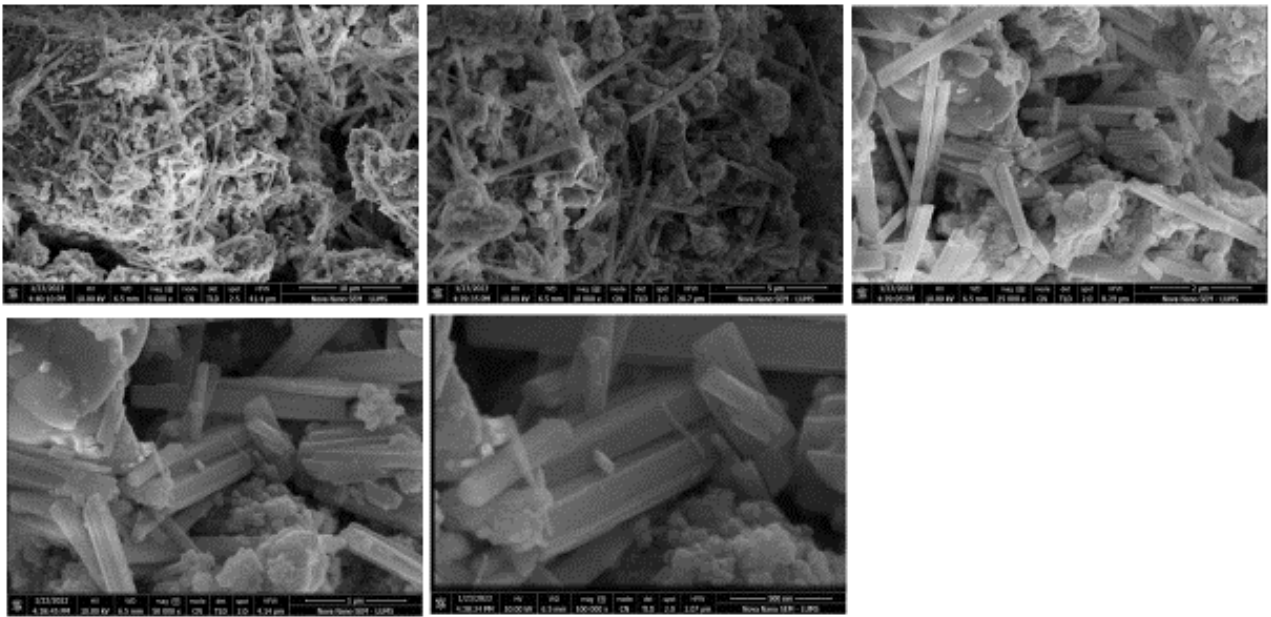


Figure 5.5. SEM images of $x=0.20$

XRD pattern as shown in Figure (3a) provides information on crystalline phases, crystallite sizes, and purity of the products $\text{Ni}_x \text{Cr}_{2-x} (\text{MoO}_4)_3$ ($x= 0, 0.05, 0.10, 0.15, \text{ and } 0.20$). All the appeared diffraction peaks in the XRD pattern of pristine Chromium Molybdate ($x=0$) correspond well to the monoclinic $\text{Cr}_2 (\text{MoO}_4)_3$ (JCPDS: 01-078-1654) in the $P21/a$ space group[62]. The diffraction peaks at $2\theta = 12.91, 13.94, 15.38, 20.57, 22.81, 23.21, 24.19, 23.92, 25.19, 25.90, 27.64, 30.33, 34.19, 37.76, \text{ and } 37.90$ are indexed to the corresponding crystallographic planes of $(-202), (200), (120), (-214), (022), (220), (-412), (-322), (-224), (222), (-402), (-404), (-116), (-521), \text{ and } (-616)$, respectively.

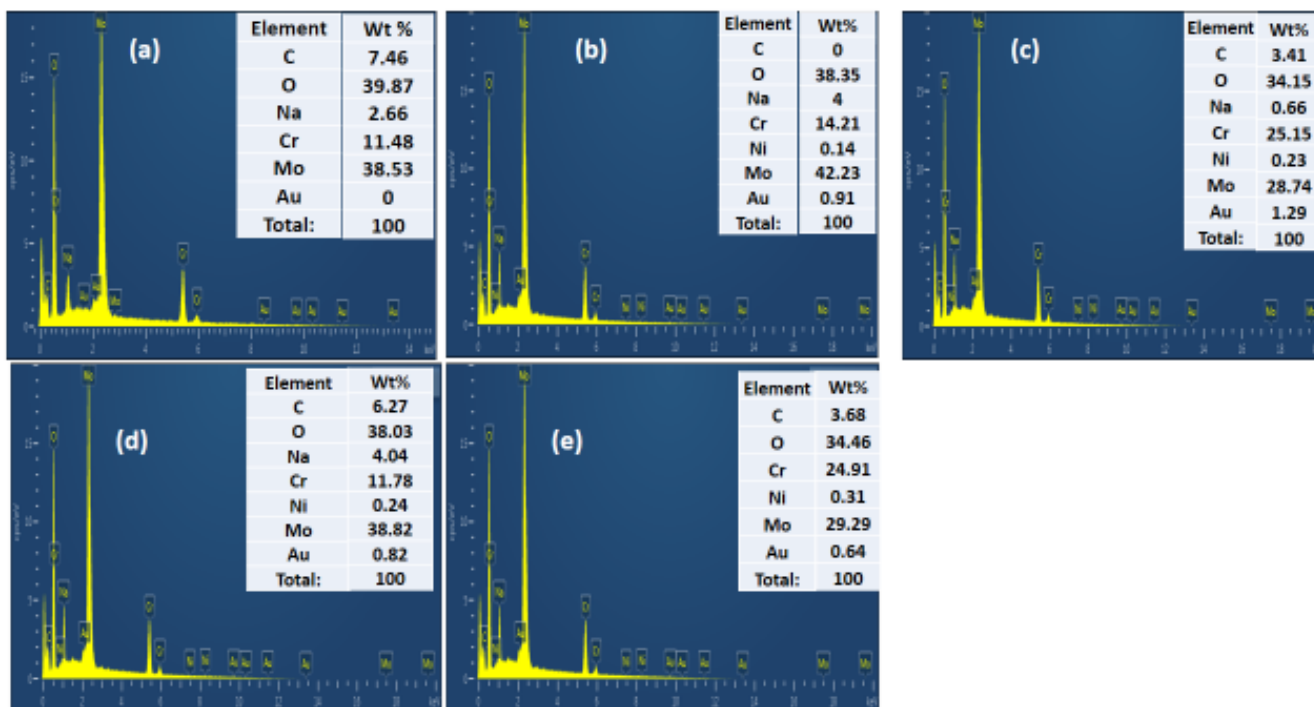


Figure 5. 6. EDS graphs of (a) $x=0$ (b) $x=0.05$ (c) $x=0.10$ (d) $x=0.15$ and (e) $x=0.20$

The diffraction pattern of $x=0.05$, 0.10 , and 0.15 exhibit the same diffraction pattern as monoclinic $\text{Cr}_2(\text{MoO}_4)_3$, indicating that incorporation of Ni into the $\text{Cr}_2(\text{MoO}_4)_3$ lattice does not change the crystal structure. However, the XRD pattern of $x=0.20$ exhibits peaks of lower intensity indicating less crystallinity. In addition to this, extra impurities peak appear which may be related to chromium oxide, molybdenum oxide, or nickel oxide. The appearance of impurity peak is due to an increase beyond the extent of doping consequently leading towards the deterioration of lattice structure. The table (S6) lists the average dimensions of crystallite determined from XRD patterns using the Scherrer formula. It is noted that the size of the crystallite decreased from 21.63 for $x=0$ to 19.56 for $x=0.20$. It is due to the doping of nickel having a smaller atomic radius than chromium, thus shrinking the lattice structure and as a result decreasing the crystallite size.

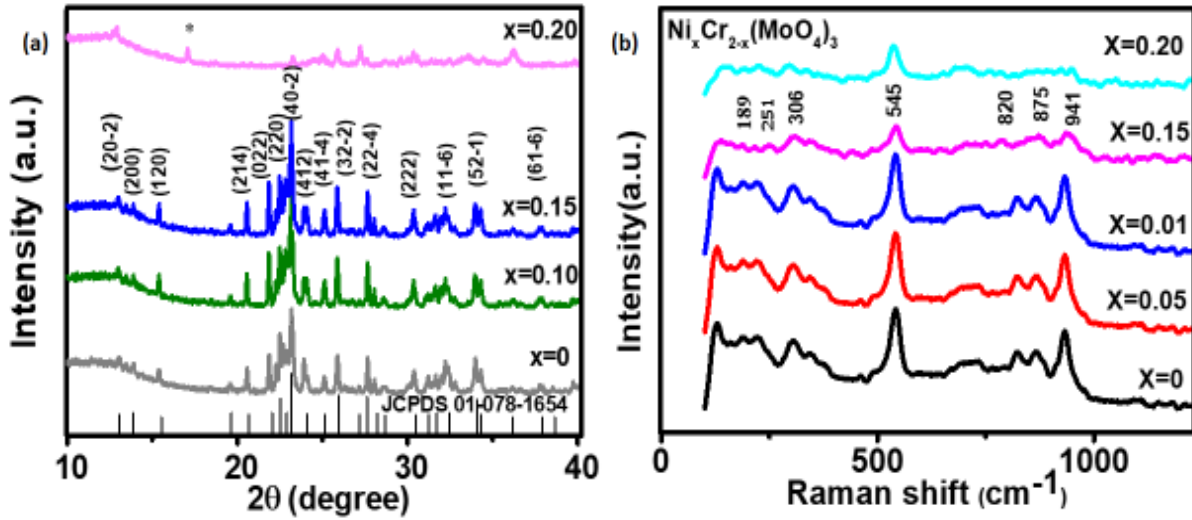


Figure 5.7. (a) XRD patterns and (b) Raman spectra of all the samples

Spectroscopy was used to further confirm the details of the structure of the samples once they had been synthesized. Figure (3b) shows the spectra of all the samples. The MoO₄ tetrahedral units' symmetric stretching mode (ν₁) and asymmetric stretching mode (ν₃), respectively, are responsible for the bands at 965 and 831. The symmetric stretching mode (ν₁) and the asymmetric stretching mode (ν₃) of Mo-O-Cr/Ni, respectively, are responsible for the bands at 941 and 748. The bands for symmetric bending (ν₂) and asymmetric bending (ν₄) of MoO₄ are present at 350 and 504, respectively [63, 64]. Raman spectra of Nickel doped samples (x=0.05, 0.10, 0.15) are in good correspondence with pristine Chromium Molybdate (x=0), thus confirming the successful doping of nickel without altering the lattice structure but the Raman bands of x=0.20 are displaced and have lower intensity, indicating changes in lattice structure and less degree of crystallinity.

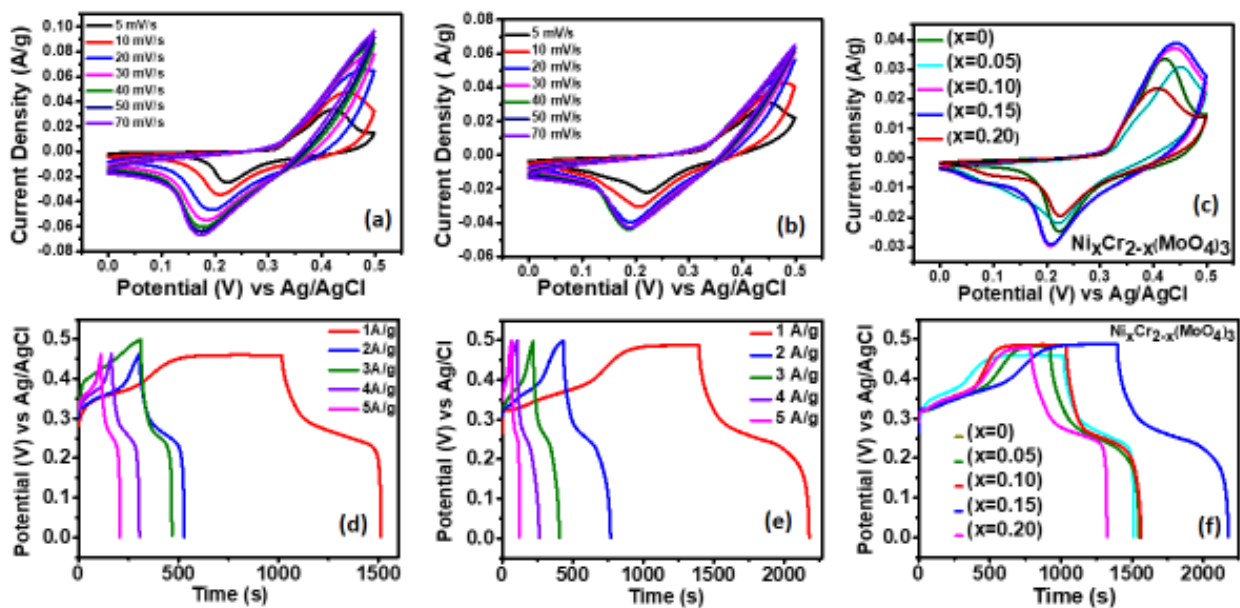


Figure 5.8. Cyclic voltammetry profiles of (a) $x=0$ (b) $x=0.20$ (c) comparative CV profiles of all the samples and GCD curves of (d) $x=0$ (e) $x=0.20$ (f) comparative GCD profiles of all the samples

s7

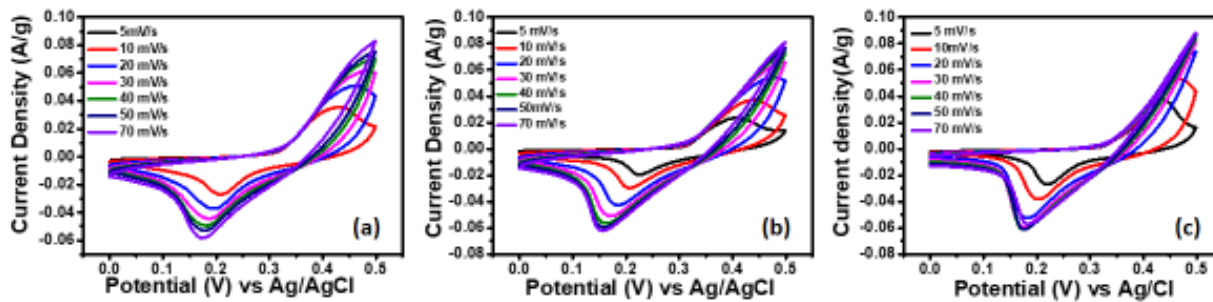


Figure 5.9. CV profiles of (a) $x=0.05$ (b) $x=0.10$ (c) $x=0.20$

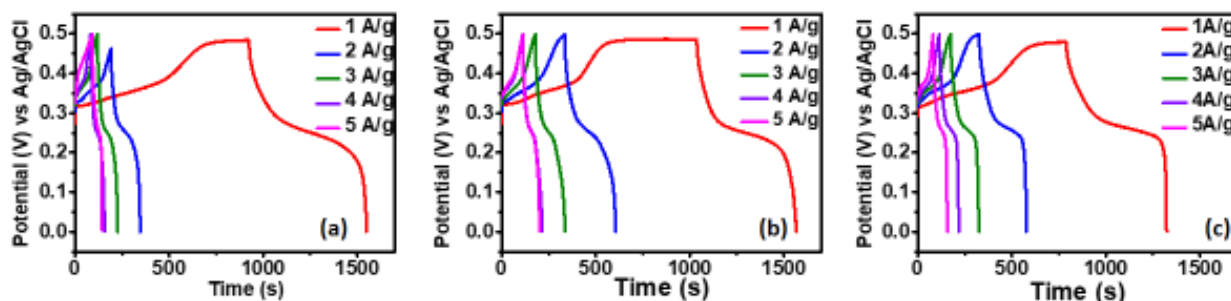


Figure 1.1.1 GCD profiles of (a) $x=0.05$ (b) $x=0.10$ (c) $x=0.20$

The suitability of prepared materials for supercapacitor applications is evaluated by performing CV, GCD, and EIS. The CV profiles of $x=0, 0.05, 0.10, 0.15,$ and 0.20 at sweep rates of $5, 10, 20, 30, 40, 50,$ and 70mVs^{-1} with a potential window of $0-0.5\text{V}$ are shown in Figures 4a, S7a, S7b, 4b, and S7c, respectively. The CV curves show that there are two peaks for redox activity that demonstrate the faradic pseudocapacitive properties. Additionally, as the rate of scanning is increased, all of the CV plots show a tiny migration in the anodic and cathodic peaks to the positive voltage and negative potential, respectively. This suggests that the electrode is CV stable and that there are quick redox events occurring at the junction of the electrode and the electrolyte. [38, 65] The comparative CV profiles of all five electrodes recorded at 5mV/sec in the potential frame of $0 - 0.5\text{V}$ are depicted in Fig 4(c) and show a pair of redox peaks for all the electrodes indicating the faradic redox reactions of $\text{Cr}^{+2}/\text{Cr}^{+3}$ with an aid of OH^- ions from the electrolyte. Moreover, the combined area under each material's CV curves, determined from comparing CV profiles increases with the doping of nickel and then decreases for $x=0.20$. Specific capacitance is calculated from

integrated areas using equation (1) and is given in Table 1. Specific capacitance for $x=0, 0.05, 0.10, 0.15,$ and 0.20 are calculated as 666, 790, 793, 828, and 695, respectively.

Table 1. Specific capacitance calculated from CV profiles of all the materials at 5 mVsec^{-1}

S. NO.	Materials $\text{Ni}_x\text{Cr}_{2-x}(\text{MoO}_4)_3$	Specific Capacitance (Fg^{-1})
1	$x=0$	666
2	$x=0.05$	790
3	$x=0.10$	793
4	$x=0.15$	828
5	$x=0.20$	695

Table 2. . Specific capacitance calculated from equation (2)

Materials	1 A/g	2 A/g	3 A/g	4 A/g	5 A/g
$x=0$	978	860	804	760	695
$x=0.05$	1092	704	660	632	600
$x=0.10$	1254	1088	972	776	712
$x=0.15$	1572	1340	1248	1200	710
$x=0.20$	1068	996	882	824	760

To further validate the results from CV, GCD were carried out at different values of current densities. Figures 4a, 4b, S8a, S8b, and S8c show the GCD plots at different current densities, values ranging from 1 to 5 Ag^{-1} for $x = (0, 0.15, 0.05, 0.10, \text{ and } 0.20)$, respectively. While the comparative graph of non-linear GCD curves of all the electrodes at 1 Ag^{-1} is depicted in Figure 1.4c. It is observed that being in correspondence with the CV profiles, all the GCD curves show distinctive voltage plateaus indicating the redox reactions and thus supporting the pseudocapacitive properties of the materials. The specific capacitance for all the materials is calculated based on equation (2) from the discharge time obtained from GCD profiles at different current densities. The values of specific capacitance are given in Table 2 and are plotted against current densities as shown in Figure (6a). All the materials exhibit the highest specific capacitance of (978, 1092, 1254, 1572, and 1068) Fg^{-1} at 1 Ag^{-1} for $x=0, 0.05, 0.10, 0.15, \text{ and } 0.20$, respectively. The results indicate two trends: (a) an increase in specific capacitance with the doping of nickel up to an extent of $x=0.15$, and then a sharp decrease for $x= 0.20$ (b) a decrease in specific capacitance with an increase in current density. Trend (a) indicates the importance of morphology, crystallite size, lattice structure, and redox reactions in the charge-storage mechanism. As evident from SEM images, the morphology changes with the addition of nickel from irregular flakes to nanorods, thus providing more surface area for the occurrence of redox reactions. Moreover, according to the average crystallite size obtained from XRD, the specific capacitance increases with the decrease in crystallite size, except for $x=0.20$ which has a lower specific capacitance despite of the smallest crystallite size. It is due to the deterioration of lattice structure as a result of doping of nickel beyond the doping extent. It can also be seen that all the Nickel doped Chromium Molybdates have higher specific capacitance than pristine Chromium Molybdate which is due to the combined effect of both Ni (II) and Cr (III) ions taking part in the redox reactions for the storage of charge. However, in trend (b), the decrease in the value of capacitance is due to different reasons including, diffusion limitation, incomplete involvement of material in the chemical reactions, and the rate of intercalation of ions at electrode/electrolyte interfaces is reduced at higher current densities thus exhibiting a short charge-discharge time and consequently smaller specific capacitance [38, 65].

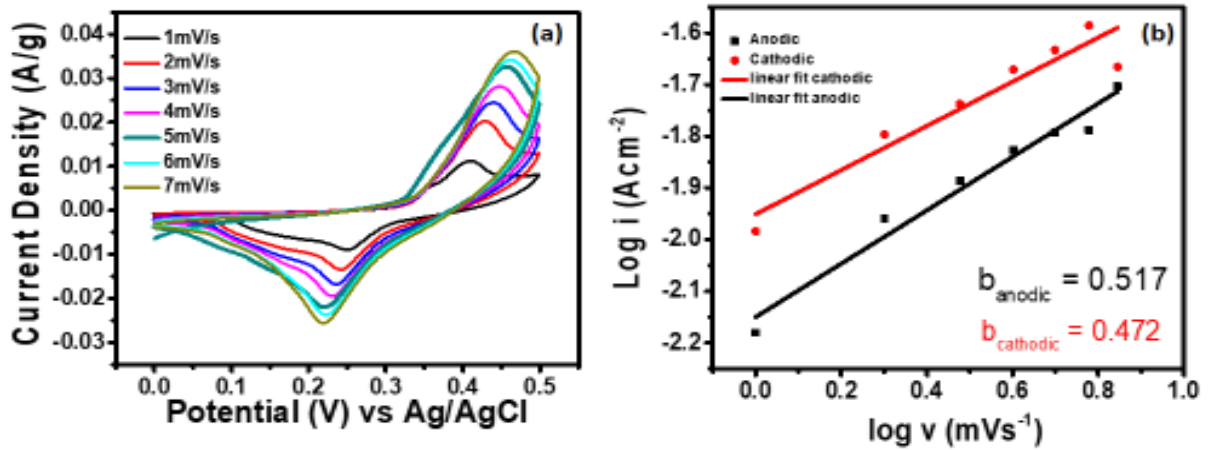


Figure 1.1.2. (a) CV recorded for kinetic studies (b) relationship between $\log i$ and $\log v$

To understand the reason behind the high specific capacitance of the samples and to study the charge-storage mechanism involved, kinetic study is performed on the material giving highest specific capacitance i.e. $x=0.15$. For this purpose, CV is recorded at 1 to 6 mVs⁻¹ in the same potential window as shown in the Figure (5a). The relationships between the anodic and cathodic peak currents (i_a and i_p) and scan rate (v) is determined from the equations (5) and (6) [66, 67] and illustrated in the Figure (5b).

$$i = av^b \quad (5)$$

$$\log i = \log a + b \log v \quad (6)$$

Where 'a' is a constant and 'b' is a parameter which is obtained from the slope of plot between $\log v$ and $\log i$. The value of b ranges from 0.5 to 1. For a diffusion-controlled (pseudo-capacitor) process, the value of b approaches to 0.5 while for surface-controlled (EDLC) process, b value is close to 1 [68]. Here, $b = 0.51$ for anodic peaks and 0.47 for cathodic peaks indicating the dominance of diffusion-controlled charge storage mechanism.

The specific capacitance values are plotted at different current densities, as shown in the Figure 6a. To explore the kinetics of the reaction, EIS was performed in the frequency range of 1 Hz to 100 kHz at open circuit potential. Figure (6b) shows the Nyquist plots of all the materials. The plots were fitted by applying an equivalent electrochemical circuit consisting of equivalent series resistance (R_s) in series with a circuit containing constant phase element (Q) in parallel with charge-transfer resistance (R_{CT}) and with another circuit containing capacitor in parallel with resistor. R_s gives an average resistance comprised of intrinsic resistance of the active material in the electrode, resistance at the interface of electrode/electrolyte and ionic resistance of electrolyte [69]. The fitting values are given in the Table S9. The results imply that by increasing the doping of nickel in materials R_s and R_{CT} increases thus decreasing the flow of charge through the circuit and consequently an increased charge storage in the capacitor. X=0.15 exhibited the highest R_{CT} of $3.67E^7$ ohm with highest capacitance of 0.00312 S. $Sec^{\wedge}n$.

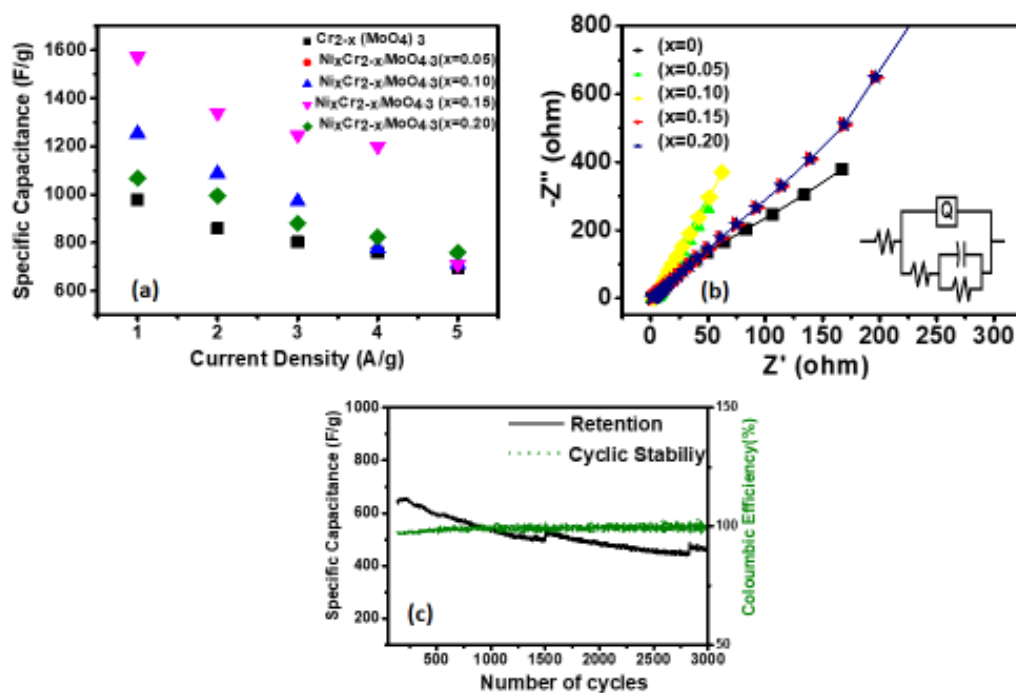


Figure 1.1.3. (a) Specific capacitance values at different current densities (b) EIS (c) Capacitance retention and Coulombic Efficiency

	Materials	Energy Density (Wh/kg) At 1 A/g	Power Density (W/kg) At 1 A/g
1.	X=0	33	244.9
2.	x=0.05	37.91	250
3.	x=0.10	43.54	249
4.	x=0.15	54.5	250
5.	x=0.20	37.08	248

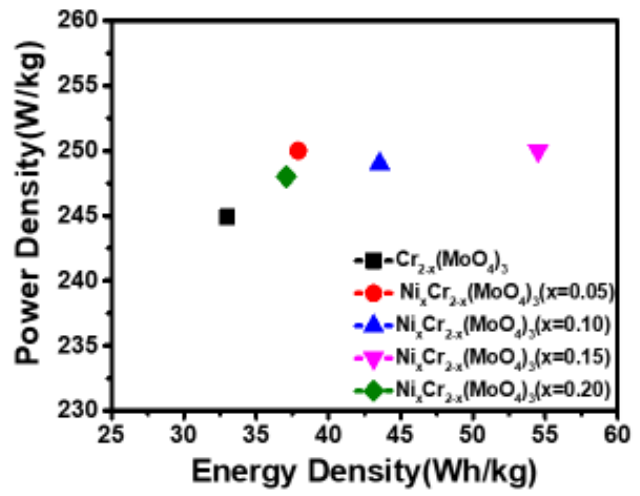


Figure 1.1.4. . Energy density and power density plot

Table 3. EIS fitting data

Materials	R_s (ohm)	CPE (S. sec ⁿ)	R_{ct} (ohm)	C (S.sec ⁵)	R (ohm)
x=0	2.017	0.00203	4.16E ³	0.0012	498.7
x=0.05	2.217	0.00319	4.34E ³	0.0031	460.3
x=0.10	2.316	0.00327	3.34E ⁴	0.0061	539.3
x=0.15	2.398	0.00411	3.67E ⁵	0.0317	668.2
x=0.20	2.14	0.00312	4.17E ³	0.0010	439.8

The stability of the best electrode is measured by performing GCD for 3000 cycles at 20 Ag^{-1} , depicted in Figure 6c. When the current density is 20 Ag^{-1} , 73% of the initial value of capacitance is retained while 100% coulombic efficiency is maintained, suggesting that the material exhibits excellent properties to be used as an anode in a supercapacitor device. Table 3 compares the present work with other binary and ternary metal oxides and composites previously reported in the literature. The comparative study shows that $\text{Ni}_x \text{Cr}_{2-x} (\text{MoO}_4)_3$ serves as a better electrode than many others. The energy density and power density are calculated using equations 3 and 4, respectively. The values are plotted as Ragone plot as shown in Figure S10.

Materials	Synthetic approach	Potential Window	Specific Capacitance	Retention	References
NiCo₂O₄	Microwave-assisted heating reflux	0.6V	1006 Fg ⁻¹ at 1 Ag ⁻¹	72.2%	[15]
TiN@FeOOH	Electro-deposition	1.2V	1564 Fg ⁻¹ at 1 Ag ⁻¹	83.5%	[70]
CuSe@Co (OH)₂	Electro-deposition	0.6V	1180 Fg ⁻¹ at 1 Ag ⁻¹	80.4%	[71]
NiMoO₄	Hydrothermal	0.5V	974 Fg ⁻¹ at 1 Ag ⁻¹	72.4%	[72]
ZnMoO₄	Microwave-assisted hydrothermal	0.5V	1212 Fg ⁻¹ at 1 Ag ⁻¹	93.5%	[73]
CuMoO₄	Sonochemical	0.5V	281 Fg ⁻¹ at 0.5 mAcm ⁻²	98%	[40]
NF@MnMoO₄	Hydrothermal	0.5V	4609 Fg ⁻¹ at 1 Ag ⁻¹	92.4%	[22]
Ni_{0.5}Co_{0.5}MoO₄	Hydrothermal	0.45V	1180 Fg ⁻¹ at 2 Ag ⁻¹	93.4%	[74]
CuCo₂O₄@	Hydrothermal	0.5V	1153 Fg ⁻¹ at 1	82.5%	[58]

MgMoO₄			Ag ⁻¹		
Ni_xCr_{2-x}(MoO₄)₃	Co-precipitation	0.5V	1572 Fg ⁻¹	73.5%	This work

Table 4 .Comparative review

CHAPTER 6: CONCLUSIONS

The monoclinic nickel doped chromium molybdates were successfully synthesized by a highly efficient, simple, and cost-effective co-precipitation technique. With the doping of nickel, the morphology was changed from nanoflakes-like in $x=0$ to nanorods in $x=0.20$, crystallite size was decreased, and the electrochemical properties were enhanced because of the structural features and the combined effect of both Ni (II) and Cr (III) ions. The pristine chromium molybdate ($x=0$) delivered the maximum specific capacitance of 978 Fg^{-1} at 1 Ag^{-1} while $x=0.15$ delivered the highest specific capacitance of 1567 Fg^{-1} at 1 Ag^{-1} with 73% of capacitance retention after 3000 cycles. All the findings suggested the potential use of the as-synthesized materials as high- performance anode material for the practical application of asymmetrical supercapacitors.

REFERENCES

1. Berardi, U.J.R., Conservation and Recycling, *A cross-country comparison of the building energy consumptions and their trends*. 2017. **123**: p. 230-241.
2. Sarwar, S., et al., *Electricity consumption, oil price and economic growth: Global perspective*. 2017. **76**: p. 9-18.
3. Benkraiem, R., et al., *The asymmetric role of shadow economy in the energy-growth nexus in Bolivia*. 2019. **125**: p. 405-417.
4. Ahmed, Z., et al., *Economic growth, renewable energy consumption, and ecological footprint: Exploring the role of environmental regulations and democracy in sustainable development*. 2022. **30**(4): p. 595-605.
5. Leonard, M.D., E.E. Michaelides, and D.N.J.R.E. Michaelides, *Energy storage needs for the substitution of fossil fuel power plants with renewables*. 2020. **145**: p. 951-962.
6. Aneke, M. and M.J.A.E. Wang, *Energy storage technologies and real life applications—A state of the art review*. 2016. **179**: p. 350-377.
7. Kim, T., et al., *Lithium-ion batteries: outlook on present, future, and hybridized technologies*. 2019. **7**(7): p. 2942-2964.
8. Feng, F., M. Geng, and D.J.I.J.o.H.E. Northwood, *Electrochemical behaviour of intermetallic-based metal hydrides used in Ni/metal hydride (MH) batteries: a review*. 2001. **26**(7): p. 725-734.
9. Ragone, D.V., *Review of battery systems for electrically powered vehicles*. 1968, SAE Technical Paper.
10. Rahman, M.M., et al., *Assessment of energy storage technologies: A review*. 2020. **223**: p. 113295.
11. Mekhilef, S., et al., *Comparative study of different fuel cell technologies*. 2012. **16**(1): p. 981-989.
12. Kirubakaran, A., et al., *A review on fuel cell technologies and power electronic interface*. 2009. **13**(9): p. 2430-2440.
13. Wang, C.-Y.J.C.r., *Fundamental models for fuel cell engineering*. 2004. **104**(10): p. 4727-4766.
14. Yan, D., et al., *NiCo₂O₄ with oxygen vacancies as better performance electrode material for supercapacitor*. 2018. **334**: p. 864-872.
15. Lei, Y., et al., *Rapid microwave-assisted green synthesis of 3D hierarchical flower-shaped NiCo₂O₄ microsphere for high-performance supercapacitor*. 2014. **6**(3): p. 1773-1780.
16. Karmakar, S., et al., *Investigation of structural and electrical transport properties of nano-flower shaped NiCo₂O₄ supercapacitor electrode materials*. 2018. **757**: p. 49-59.
17. Xu, L., et al., *Morphology controlled preparation of ZnCo₂O₄ nanostructures for asymmetric supercapacitor with ultrahigh energy density*. 2017. **123**: p. 296-304.
18. Zhou, G., et al., *Simple method for the preparation of highly porous ZnCo₂O₄ nanotubes with enhanced electrochemical property for supercapacitor*. 2014. **123**: p. 450-455.
19. Dong, Y., et al., *Facile synthesis of hierarchical nanocage MnCo₂O₄ for high performance supercapacitor*. 2017. **225**: p. 39-46.
20. Wang, H., et al., *Three-dimensional MnCo₂O₄/graphene composites for supercapacitor with promising electrochemical properties*. 2019. **792**: p. 122-129.
21. Nagamuthu, S., et al., *Hybrid supercapacitor devices based on MnCo₂O₄ as the positive electrode and FeMn₂O₄ as the negative electrode*. 2016. **390**: p. 202-208.
22. Xu, Z., et al., *High-Energy-Density Asymmetric Supercapacitor Based on a Durable and Stable Manganese Molybdate Nanostructure Electrode for Energy Storage Systems*. ACS Applied Energy Materials, 2020. **3**(6): p. 5393-5404.
23. Arsent'ev, M.Y., et al., *NiMn₂O₄ spinel as a material for supercapacitors with a pseudocapacity effect*. 2017. **43**(4): p. 376-379.
24. Wang, F., et al., *Spinel LiMn₂O₄ nanohybrid as high capacitance positive electrode material for supercapacitors*. 2014. **246**: p. 19-23.
25. Lin, Y.-P. and N.-L.J.J.o.P.S. Wu, *Characterization of MnFe₂O₄/LiMn₂O₄ aqueous asymmetric supercapacitor*. 2011. **196**(2): p. 851-854.

26. Mola, B.A., et al., *Design and construction of hierarchical MnFe₂Ce₄@ MnNiCe₄ nanosheets on Ni foam as an advanced electrode for battery-type supercapacitor applications*. 2022. **51**: p. 104542.
27. Ansari, S.A., et al., *Development of binder free interconnected 3D flower of NiZn₂O₄ as an advanced electrode materials for supercapacitor applications*. 2021. **12**(1): p. 14.
28. Mu, X., et al., *A high energy density asymmetric supercapacitor from ultrathin manganese molybdate nanosheets*. 2016. **211**: p. 217-224.
29. Abdah, M.A.A.M., et al., *Review of the use of transition-metal-oxide and conducting polymer-based fibres for high-performance supercapacitors*. 2020. **186**: p. 108199.
30. Bulakhe, R.N., A.B. Bhalerao, and I. In, *Mixed transition metal oxides for energy applications*, in *Chemically Deposited Nanocrystalline Metal Oxide Thin Films*. 2021, Springer. p. 405-429.
31. Senthilkumar, B., et al., *Synthesis and characterization of manganese molybdate for symmetric capacitor applications*. 2015. **10**(1): p. 185-193.
32. Wang, J., et al., *A high energy asymmetric supercapacitor based on flower-like CoMoO₄/MnO₂ heterostructures and activated carbon*. 2016. **213**: p. 663-671.
33. Hussain, S., et al., *Novel gravel-like NiMoO₄ nanoparticles on carbon cloth for outstanding supercapacitor applications*. 2020. **46**(5): p. 6406-6412.
34. Guo, D., et al., *Facile synthesis and excellent electrochemical properties of CoMoO₄ nanoplate arrays as supercapacitors*. 2013. **1**(24): p. 7247-7254.
35. Xia, X., et al., *One-step synthesis of CoMoO₄/graphene composites with enhanced electrochemical properties for supercapacitors*. 2013. **99**: p. 253-261.
36. Li, P., et al., *A high-performance asymmetric supercapacitor electrode based on a three-dimensional ZnMoO₄/CoO nanohybrid on nickel foam*. 2019. **11**(28): p. 13639-13649.
37. Xu, X., et al., *Metal-organic framework-derived ZnMoO₄ nanosheet arrays for advanced asymmetric supercapacitors*. 2020. **31**(4): p. 3631-3641.
38. Gao, Y.-P., et al., *High-performance symmetric supercapacitor based on flower-like zinc molybdate*. 2018. **731**: p. 1151-1158.
39. Seevakan, K., et al., *Structural, morphological and magneto-optical properties of CuMoO₄ electrochemical nanocatalyst as supercapacitor electrode*. 2018. **44**(16): p. 20075-20083.
40. Ali, N.U.H.L., et al., *CuMoO₄ nanostructures: A novel bifunctional material for supercapacitor and sensor applications*. 2022. **52**: p. 104784.
41. Veerasubramani, G.K., et al., *Sonochemical synthesis, characterization, and electrochemical properties of MnMoO₄ nanorods for supercapacitor applications*. 2014. **147**(3): p. 836-842.
42. Purushothaman, K., M. Cuba, and G.J.M.R.B. Muralidharan, *Supercapacitor behavior of α-MnMoO₄ nanorods on different electrolytes*. 2012. **47**(11): p. 3348-3351.
43. Karthikeyan, S., et al., *Supercapacitor: Evolution and review*. 2021. **46**: p. 3984-3988.
44. Veerasubramani, G.K., K. Krishnamoorthy, and S.J.J.R.a. Kim, *Electrochemical performance of an asymmetric supercapacitor based on graphene and cobalt molybdate electrodes*. 2015. **5**(21): p. 16319-16327.
45. Seevakan, K., et al., *Electrochemical and magneto-optical properties of cobalt molybdate nano-catalyst as high-performance supercapacitor*. 2018. **44**(15): p. 17735-17742.
46. Wu, Y., et al., *Facile synthesis of novel Zn₅Mo₂O₁₁·5H₂O nanoflowers with excellent rate capability in supercapacitors*. 2022. **520**: p. 230816.
47. Yu, T., et al., *Facile synthesis of flowerlike Bi₂MoO₆ hollow microspheres for high-performance supercapacitors*. 2018. **6**(6): p. 7355-7361.
48. Farahpour, M. and M.J.N.J.o.C. Arvand, *In situ synthesis of advantageously united copper stannate nanoparticles for a new high powered supercapacitor electrode*. 2022. **46**(8): p. 3806-3816.
49. Xu, C., et al., *Controllable design of polypyrrole-iron oxide nanocoral architectures for supercapacitors with ultrahigh cycling stability*. 2019. **2**(3): p. 2161-2168.
50. Deyab, N.M., M.M. Taha, and N.K.J.N.A. Allam, *A mesoporous ternary transition metal oxide nanoparticle composite for high-performance asymmetric supercapacitor devices with high specific energy*. 2022. **4**(5): p. 1387-1393.
51. Nakate, U.T., et al., *Ultrathin ternary metal oxide Bi₂MoO₆ nanosheets for high performance asymmetric supercapacitor and gas sensor applications*. 2021. **551**: p. 149422.
52. Raj, B.G.S., H.-Y. Kim, and B.-S.J.E.A. Kim, *Ultrasound assisted formation of Mn₂SnO₄ nanocube as electrodes for high performance symmetrical hybrid supercapacitors*. 2018. **278**: p. 93-105.

53. Sahoo, A., Y.J.M.C. Sharma, and Physics, *Synthesis and characterization of nanostructured ternary zinc manganese oxide as novel supercapacitor material*. 2015. **149**: p. 721-727.
54. Sahoo, S., S. Zhang, and J.-J.J.E.A. Shim, *Porous ternary high performance supercapacitor electrode based on reduced graphene oxide, NiMn₂O₄, and polyaniline*. 2016. **216**: p. 386-396.
55. Cai, D., et al., *Comparison of the electrochemical performance of NiMoO₄ nanorods and hierarchical nanospheres for supercapacitor applications*. 2013. **5**(24): p. 12905-12910.
56. Chavan, H.S., et al., *Nanoflake NiMoO₄ based smart supercapacitor for intelligent power balance monitoring*. 2018. **185**: p. 166-173.
57. Gao, H., et al., *A simple fabrication, microstructure, optical, photoluminescence and supercapacitive performances of MgMoO₄/MgWO₄ heterojunction micro/nanocomposites*. 2022. **129**: p. 106909.
58. Hao, C., et al., *Fabrication of flower-shaped CuCo₂O₄@ MgMoO₄ nanocomposite for high-performance supercapacitors*. 2021. **41**: p. 102972.
59. Xu, X., et al., *Microwave-assisted synthesis of graphene/CoMoO₄ nanocomposites with enhanced supercapacitor performance*. 2014. **616**: p. 58-65.
60. Ghosh, D., et al., *α MnMoO₄/graphene hybrid composite: high energy density supercapacitor electrode material*. 2014. **43**(28): p. 11067-11076.
61. Vernon-Parry, K.D.J.I.-V.R., *Scanning electron microscopy: an introduction*. 2000. **13**(4): p. 40-44.
62. Oudghiri-Hassani, H.J.J.M.E.S., *Synthesis, characterization and application of chromium molybdate for oxidation of methylene blue dye*. 2018. **9**(3): p. 1051-1057.
63. Nti, F., et al., *Facilely synthesized NiMoO₄/CoMoO₄ nanorods as electrode material for high performance supercapacitor*. 2018. **742**: p. 342-350.
64. Battle, P., et al., *The structure and magnetic properties of chromium (III) molybdate*. 1985. **58**(2): p. 221-225.
65. Pang, M., et al., *Comparison of α -NiMoO₄ nanorods and hierarchical α -NiMoO₄@ δ -MnO₂ core-shell hybrid nanorod/nanosheet aligned on Ni foam for supercapacitors*. 2017. **708**: p. 14-22.
66. Xu, Z., et al., *High-energy-density asymmetric supercapacitor based on a durable and stable manganese molybdate nanostructure electrode for energy storage systems*. 2020. **3**(6): p. 5393-5404.
67. Pu, X., et al., *Understanding and calibration of charge storage mechanism in cyclic voltammetry curves*. 2021. **133**(39): p. 21480-21488.
68. Yu, D., et al., *Synthesis of transition metal cation decorated nickel molybdate nanoarrays on nickel foam and their applications in high-performance battery-supercapacitor hybrid devices*. 2021. **884**: p. 161092.
69. Mei, B.-A., et al., *Physical interpretations of electrochemical impedance spectroscopy of redox active electrodes for electrical energy storage*. 2018. **122**(43): p. 24499-24511.
70. Niu, D., et al., *FeOOH Composite Electrode Based on TiN Nanopetals for High-Performance Supercapacitors*. *The Journal of Physical Chemistry C*, 2020. **124**(28): p. 15028-15035.
71. Gong, J., et al., *High-Performance Flexible All-Solid-State Asymmetric Supercapacitors Based on Vertically Aligned CuSe@Co(OH)₂ Nanosheet Arrays*. *The Journal of Physical Chemistry C*, 2018. **122**(4): p. 2002-2011.
72. Cai, D., et al., *Comparison of the Electrochemical Performance of NiMoO₄ Nanorods and Hierarchical Nanospheres for Supercapacitor Applications*. *ACS Applied Materials & Interfaces*, 2013. **5**(24): p. 12905-12910.
73. Xu, X., et al., *Metal-organic framework-derived ZnMoO₄ nanosheet arrays for advanced asymmetric supercapacitors*. 2020. **31**: p. 3631-3641.
74. Denis, D.K., et al., *Rate Balance Design and Construction of a Conductive Ni_{0.5}Co_{0.5}MoO₄ Solid-Solution Microspherical Superstructure toward Advanced Hybrid Supercapacitors*. *ACS Applied Energy Materials*, 2021. **4**(9): p. 9470-9478.